

## Age distributions and dynamically changing hydrologic systems: Exploring topography-driven flow

J. D. Gomez<sup>1</sup> and J. L. Wilson<sup>1</sup>

Received 18 September 2012; revised 31 January 2013; accepted 5 February 2013; published 20 March 2013.

[1] Natural systems are driven by dynamic forcings that change in time as well as space, behavior that is inherited by the system flow field and results in time-varying age distributions (ADs). This work presents a review of the mathematical tools and solution approaches used to model ADs in dynamic time-varying flow systems. A simple conceptual, numerical model is then used to explore the role of flow dynamics in ADs for topography-driven flow systems. This model is an analog for regional groundwater systems and hyporheic zones. This model demonstrates that relatively small fluctuations in the forcing, even though importantly affecting the flow in the system, can have minimal effects in ADs. However, as the intensity of fluctuation increases, still within the bounds observed in natural systems, ADs in shallow parts of the system become highly sensitive to dynamic flow conditions, leading to considerable changes in the moments and modality of the distributions with time. In particular, transient flow can lead to emergence of new modes in the AD, which would not be present under steady flow conditions. The discrepancy observed between ADs under steady and transient flow conditions is explained by enhancement of mixing due to temporal variations in the flow field. ADs in deeper parts of the system are characterized by multimodality and tend to be more stable over time even for large forcing fluctuations.

**Citation:** Gomez, J. D., and J. L. Wilson (2013), Age distributions and dynamically changing hydrologic systems: Exploring topography-driven flow, *Water Resour. Res.*, 49, 1503–1522, doi:10.1002/wrcr.20127.

### 1. Introduction

[2] Age distributions (ADs) are space- and time-dependent deterministic distributions that provide an integrated measure of the flow and transport characteristics of natural hydrologic systems. ADs vary in space, with positions further along flow paths exhibiting older ages. In particular, ADs represent the time of exposure of water and its constituents to the system's chemical conditions and are therefore a key control on the transformations taking place. If the hydrologic flow system is in steady state, the flow paths do not change in time, and water present at a given point has a stable AD, but if the flow field changes so does the AD. For the purpose of this paper, we focus on subsurface systems (groundwater aquifers and stream hyporheic zones (HZs)) with transient flows, changing flow paths, and transient ADs. The AD concept is ubiquitous and well established in areas including biology [e.g., *Trucco*, 1965; *Rotenberg*, 1972], chemical engineering [e.g., *Fogler*, 2006], atmospheric science [e.g., *Bolin and Rodhe*, 1973; *Hall and Plumb*, 1994; *Holzer and Hall*, 2000], physical oceanogra-

phy [e.g., *Haine and Hall*, 2002; *Delhez et al.*, 2002; *Haine et al.*, 2008], and hydrologic sciences [e.g., *Campana*, 1987; *Jury and Roth*, 1990; *Goode*, 1996; *Varni and Carrera*, 1998; *Ginn*, 1999; *Cornaton and Perrochet*, 2006a].

[3] Groundwater age is widely used as a tool in applications such as the assessment of aquifer renewability, replenishment, and vulnerability [e.g., *Fogg et al.*, 1999; *Zongyu et al.*, 2005], identification of groundwater flow paths [e.g., *Price et al.*, 2003; *Pint et al.*, 2003], estimation of aquifer properties and groundwater velocities [e.g., *Sturchio et al.*, 2004], and estimation of recharge rates [e.g., *Xu and Beekman*, 2003]. Both measured and modeled groundwater ages are usually treated as if the flow field and ADs are time invariant [e.g., *Goode*, 1996; *Haggerty et al.*, 2002; *McGuire and McDonnell*, 2006; *Cornaton and Perrochet*, 2006a; *Cardenas*, 2007; *Fiori and Russo*, 2008; *Bethke and Johnson*, 2008], ignoring the potential effects of past and future variability of weather, climate, and other natural and human forcings. However, hydrologic flow paths and ADs can change dynamically with the temporal variability of these forcings. Regional groundwater systems (RGSs), deep vadose zones, hillslopes, and stream HZs are examples of dynamic hydrologic systems driven by forcings varying at several time scales, such as daily, seasonal, interannual, decadal, and longer.

[4] There are two approaches to estimate groundwater ages: (i) the use of environmental tracers as a proxy for groundwater age and (ii) mathematical modeling of groundwater age. These tools must be applied in tandem

<sup>1</sup>Department of Earth and Environmental Science, New Mexico Institute of Mining and Technology, Socorro, New Mexico, USA.

Corresponding author: J. D. Gomez, Department of Earth and Environmental Science, New Mexico Institute of Mining and Technology, MSEC 216, Socorro, NM 87801, USA. (jdgomez@nmt.edu)

to better characterize natural hydrologic systems. The first one relies on the use of known decay rates of radioactive isotopes, the timing of introduction into the atmosphere of isotopes from nuclear testing or reactors, or the history of the release of manufactured gases to estimate the age of the groundwater sample [Bethke and Johnson, 2008]. The main concern about this approach deals with the interpretation of an estimated age value, since it is not always clear if it represents the mean age, a particular mode of the AD, or just a misleading value due to mixing effects. The estimated age is certainly instructive and useful, particularly for simple flow systems without strong mixing, but it does not provide much information about the actual AD, which may be quite complex and cover a wide variety of age values, depending on the system's nature and hydrodispersive components [Kazemi et al., 2006]. Reviews of environmental tracer age dating techniques, their applications, and drawbacks can be found in Clark and Fritz [1997], Phillips and Castro [2003], and Kazemi et al. [2006].

[5] Mathematical modeling based on the solution of age transport equations is an alternative that allows the reconstruction of the ADs or its moments. However, it requires a full understanding of the hydrodynamics of the flow system, which means knowing the flow field, the propensity for sequestration in low-permeability materials (e.g., aquitards), and the dispersive properties at every location and time. Different modeling approaches have been used, but the common assumption is that the flow system is steady [Goode, 1996; Varni and Carrera, 1998; Etcheverry and Perrochet, 2000; Weissmann et al., 2002; McGuire and McDonnell, 2006].

[6] In this paper we review the main tools available to mathematically model ADs in dynamically changing hydrologic systems and present three different mathematical solution approaches to efficiently implement these tools (section 2). Even though flow dynamics has been recognized as an important aspect on age analyses, it has only been partially explored with a theoretical approach similar to that used in this paper [e.g., Woolfenden and Ginn, 2009; Massoudieh and Ginn, 2011; Cornaton, 2012]. Alternative theoretical approaches, such as reservoir theory, have been presented for steady flow [Cornaton and Perrochet, 2006a, 2006b] while commenting on the possibility to extend the theory to transient flow, but to the authors' knowledge it has not yet been investigated. We then explore the importance of transient forcing on ADs by using a conceptual model for topography-driven flow where the forcing evolves over time leading to time-varying flow paths (sections 3 and 4). This model is an analog for flow in RGSs where the water table is a subdued replica of the topography and HZs where flow is driven by local head gradients created by channel slope discontinuities.

## 2. Groundwater Age Modeling

[7] Ginn [1999] introduced a mathematical model that describes the exposure time (or age) of a mixture constituent (e.g., water, solute, or colloid). In this model, the constituent bulk-phase mass density  $c(\mathbf{x}, t, \tau)$  is a function of the position vector  $\mathbf{x} = (x, y, z)$  at any point

in the domain  $\Omega$ , time  $t$ , and age  $\tau$  ( $\tau \geq 0$ ), which is described by the following partial differential equation (PDE):

$$\frac{\partial(\theta c)}{\partial t} + \mathcal{G}(c) + v_r \theta \frac{\partial c}{\partial \tau} = r. \quad (1)$$

[8] Equation (1), which ignores sequestration in low-permeability materials, is analogous to the advection-dispersion equation (ADE) but in a 5-D space (3-D space-time-age), where  $\mathbf{v}(\mathbf{x}, t) = (v_x, v_y, v_z)$  is the pore velocity,  $\theta(\mathbf{x}, t)$  is the porosity,  $v_r$  is the rate of change of a material point location on the age axis per unit time,  $r(\mathbf{x}, t, \tau)$  is the rate of transformation due to reactions, and  $\mathcal{G}(c) = \nabla \cdot (\mathbf{v}\theta c) - \nabla \cdot (\theta \mathbf{D} \nabla c)$  is the transport operator that, in this example, includes advection and Fickian diffusion and dispersion. Notice that this operator can be nonlocal as recently explored by Engdahl et al. [2012]. The dispersion-diffusion tensor  $\mathbf{D} = \{D_{ij}\}$  is defined as [Bear, 1972]:

$$D_{ij} = (\alpha_T |\mathbf{v}| \delta_{ij}) + [(\alpha_L - \alpha_T) / v_i v_j |\mathbf{v}|] + D_m \quad (2)$$

with  $\alpha_T$  and  $\alpha_L$  the transverse and longitudinal dispersivities,  $D_m$  the effective molecular self-diffusion coefficient, and  $\delta_{ij}$  the Kronecker delta function.

[9] The conventional mass density can be expressed as

$$c_T(\mathbf{x}, t) = \int_0^\infty c(\mathbf{x}, t, \xi) d\xi, \quad (3)$$

and satisfies the traditional ADE:

$$\frac{\partial(\theta c_T)}{\partial t} + \mathcal{G}(c_T) = \int_0^\infty r(\mathbf{x}, t, \xi) d\xi. \quad (4)$$

[10] The age density or AD splits the density of a constituent into continuous age classes. The age density function  $\rho(\mathbf{x}, t, \tau)$ , defined as positive definite, represents the contribution of material with an age  $\tau$  to the conventional mass density  $c_T(\mathbf{x}, t)$  so that

$$\rho(\mathbf{x}, t, \tau) = \frac{c(\mathbf{x}, t, \tau)}{c_T(\mathbf{x}, t)} \quad (5)$$

and  $\int_0^\infty \rho(\mathbf{x}, t, \xi) d\xi = 1$ .

[11] If the constituent of interest is water ( $v_r = 1$ ), and assuming that its density remains essentially constant (e.g.,  $c_T(\mathbf{x}, t) \sim 1000 \text{ kg m}^{-3}$  for incompressible flows and SI units), the AD  $\rho$  satisfies the PDE [Ginn, 1999]

$$\frac{\partial(\theta \rho)}{\partial t} + \mathcal{G}(\rho) + \theta \frac{\partial \rho}{\partial \tau} = S, \quad (6)$$

where the term  $S(\mathbf{x}, t, \tau)$  in equation (6) can be used to represent internal sources (e.g., recharge) or sinks (e.g.,

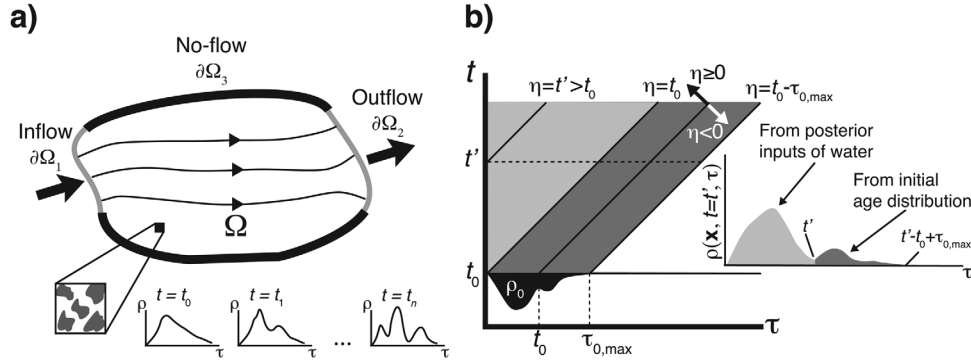


**Figure 1.** (a) Schematic representation of the domain  $\Omega$ . Boundaries are defined by the flow field as: (i) inflow ( $\partial\Omega_1$ ), (ii) outflow ( $\partial\Omega_2$ ), and (iii) no flow ( $\partial\Omega_3$ ). The size and location of  $\partial\Omega_1$ ,  $\partial\Omega_2$ , and  $\partial\Omega_3$  can change in a dynamic system. The lower portion of Figure 1 illustrates the temporal evolution of the AD at a particular location (REV) in the domain. (b) Mapping  $(\tau, t) \rightarrow (\eta = t - \tau, t)$  at a location  $\mathbf{x}$ . The image illustrates the  $(\tau, t)$  domain, where information is traveling along the characteristics  $\eta$ . At a particular time  $t'$ , the AD at this location has contributions from both the initial AD and later inputs of water. In this case, the initial AD  $\rho_0(\mathbf{x}, \tau)$  represents water molecules with ages in the interval  $[0, \tau_{0,\max}]$ , and its contributions travel along the characteristics  $\eta \in [t_0 - \tau_{0,\max}, t_0]$  as illustrated by the dark gray area in Figure 1. Similarly, information corresponding to later inputs of fresh water travels along  $\eta \geq t_0$ . Eventually, the effect of the initial distribution vanishes.

withdrawals). This expression is known as the governing equation for groundwater age (GWAE) in the hydrology literature, and as demonstrated by *Ginn et al.* [2009], it encapsulates previous equations for the transport of different measures of age such as the mean age equation [Goode, 1996], the percentile age, and moment equation [Varni and Carrera, 1998], and with the addition of sequestration in low-permeability materials the equation that describes the ages in a dual aquifer-aquitard system (aquitard age equation) [Bethke and Johnson, 2002, 2008].

[12] The initial condition for age density in the time dimension,  $\rho_0(\mathbf{x}, \tau)$ , is generally unknown and depends on the system's geological evolution, presence of formation water, and flow history. In this regard, the influence of formation water is particularly important in geologically recent aquifers (e.g., poorly lithified sedimentary formations with zones of a low-permeability material) where the initial condition becomes more important and uncertain [Varni and Carrera, 1998]. The example presented in section 3 uses a transient forcing in spin-up mode until the starting ADs are unimportant and a dynamic equilibrium is obtained. Then, an initial condition is reached and expressed mathematically as

$$\rho(\mathbf{x}, t = t_0, \tau) = \rho_0(\mathbf{x}, \tau), \quad (7)$$

where  $t_0$  is an arbitrary time at which we start the analysis. Also, this is an initial value problem in the age dimension with the initial condition given by

$$\rho(\mathbf{x}, t, \tau = 0) = 0. \quad (8)$$

[13] Flow within a natural reservoir (see Figure 1a) is characterized by inflow ( $\partial\Omega_1$ ), outflow ( $\partial\Omega_2$ ), and no-flow ( $\partial\Omega_3$ ) boundaries, as well as internal sources and sinks. To model the evolution of ADs within the system, boundary

conditions and source/sink terms must be specified. These depend on the flow characteristics, application, features to be highlighted, and the direction of flow. For instance, let  $\rho_I(\mathbf{x}, t, \tau)$  and  $\rho_S(\mathbf{x}, t, \tau)$  be the ADs of incoming water flowing through an inflow boundary (e.g.,  $\partial\Omega_1$  in Figure 1a) and source (e.g., recharge or an injection well), respectively. In this case, the inflow boundary is treated as prescribed or Dirichlet with  $\rho(\mathbf{x}, t, \tau) = \rho_I(\mathbf{x}, t, \tau)$  on  $\partial\Omega_1$ . The source terms are defined as  $S = Q_{\text{in}} \delta(\mathbf{x} - \mathbf{x}_S) \rho_S(\mathbf{x}, t, \tau)$ , where  $Q_{\text{in}}$  is the rate at which water enters the system at  $\mathbf{x}_S$ . For the particular case in which the age is defined as the time since water entered the system (e.g., ignoring residence time in the vadose zone), the inflow and source ADs are concentrated at zero and mathematically described by a delta Dirac function,  $\rho_I(\mathbf{x}, t, \tau) = \rho_S(\mathbf{x}, t, \tau) = \delta(\tau)$ . Then, for example, the effect of recharge  $Q_{\text{in}}$  is included as  $S = Q_{\text{in}} \delta(\mathbf{x} - \mathbf{x}_S) \delta(\tau)$ . Similarly, the sink term for water leaving the system at a rate  $Q_{\text{out}}$  (e.g., a pumping well) is described by  $S = Q_{\text{out}} \delta(\mathbf{x} - \mathbf{x}_S) \rho(\mathbf{x}_S, t, \tau)$ . Water leaving the system through an outflow boundary (e.g.,  $\partial\Omega_2$  in Figure 1a) has an AD dictated by an advective boundary condition (see equation (9c)).

### 2.1. Solution of the GWAE

[14] A complete mathematical statement for modeling groundwater age in a general domain, ignoring sequestration in low-permeability materials and without internal sources or sinks (see Figure 1a), is

$$\frac{\partial(\theta\rho)}{\partial t} + \mathcal{G}(\rho) + \theta \frac{\partial\rho}{\partial\tau} = 0 \quad (9a)$$

$$\rho(\mathbf{x}, t, \tau) = \delta(\tau) \quad \text{on} \quad \partial\Omega_1 \quad (9b)$$

$$\mathbf{n} \cdot (\theta \mathbf{D} \nabla \rho) = 0 \quad \text{on} \quad \partial\Omega_2 \quad (9c)$$

$$\mathbf{n} \cdot (\mathbf{v}\theta\rho - \theta\mathbf{D}\nabla\rho) = 0 \quad \text{on } \partial\Omega_3 \quad (9d)$$

$$\rho(\mathbf{x}, t, \tau = 0) = 0 \quad (9e)$$

$$\rho(\mathbf{x}, t = t_0, \tau) = \rho_0(\mathbf{x}, \tau), \quad (9f)$$

where  $\mathbf{n}$  is the unit normal vector at the boundary. This model simplifies for steady-state flow ( $\mathcal{G}$  has no time dependence) since the age density no longer depends on time ( $\rho(\mathbf{x}, t, \tau) = \rho(\mathbf{x}, \tau)$ ). Then, the derivative with respect to time in equation (9a) and the initial condition in time, expressed in equation (9f), disappear, leading to the traditional ADE with time replaced by age [Ginn, 1999]. It is important to notice that the cumulative AD,  $R(\mathbf{x}, t, \tau) = \int_0^\tau \rho(\mathbf{x}, t, \xi) d\xi$ , is described by the same mathematical statement as  $\rho$ , changing the right-hand side of equations (9b) and (9f) to the Heaviside step function  $H(\tau)$  and  $\int_0^\tau \rho_0(\mathbf{x}, \xi) d\xi$ , respectively.

[15] Finally, we introduce the moments of the AD. In general, a full description of the AD based on its moments is not feasible, because its functional form is not known a priori [Campana, 1987], and natural systems are commonly characterized by multimodal distributions [Cornaton and Perrochet, 2006a]. However, moments can be used as a tool to evaluate the importance of flow dynamics on the evolution of ADs and the time taken by the system to reach a dynamic equilibrium. The moments of  $\rho$  can be estimated as

$$a_n(\mathbf{x}, t) = \int_0^\infty \xi^n \rho(\mathbf{x}, t, \xi) d\xi. \quad (10)$$

[16] Then, it can be shown that for  $n=1, 2, \dots$  and  $a_0(\mathbf{x}, t) = 1$  [e.g., Varni and Carrera, 1998; Ginn, 1999]

$$\frac{\partial(\theta a_n)}{\partial t} + \mathcal{G}(a_n) = n\theta a_{n-1} \quad (11a)$$

$$a_n(\mathbf{x}, t) = 0 \quad \text{on } \partial\Omega_1 \quad (11b)$$

$$\mathbf{n} \cdot (\theta\mathbf{D}\nabla a_n) = 0 \quad \text{on } \partial\Omega_2 \quad (11c)$$

$$\mathbf{n} \cdot (\mathbf{v}\theta a_n - \theta\mathbf{D}\nabla a_n) = 0 \quad \text{on } \partial\Omega_3 \quad (11d)$$

$$a_n(\mathbf{x}, t = t_0) = a_{n0} = \int_0^\infty \xi^n \rho_0(\mathbf{x}, \xi) d\xi. \quad (11e)$$

[17] Moments can be directly derived via equations (11) or by integrating equation (10) given the age density derived via equations (9).

[18] There are different approaches to explore the evolution of age density for transient flow systems. The challenge is to solve a 5-D PDE (equation (9a)), a complicated task from the analytical and numerical points of view. One approach to reduce dimensionality is to solve the moment expressions (11) for several orders; however, this limits the description of the AD as mentioned before and becomes cumbersome as we increase the order of the moments. In the following subsections, we present three other approaches to solve for the full distribution that can be eas-

ily and efficiently implemented in common transport codes. First, we present an approach that uses a change of variables to simplify the mathematical statement, which becomes a series of independent advection-dispersion problems driven by slightly different boundary and initial conditions. Second, Laplace transforms are used to reduce dimensionality [Cornaton, 2012]. And finally, we mention the use of an extra spatial dimension to represent the age dimension. Even though all approaches are feasible, the example presented later in this paper uses the first one.

### 2.1.1. Change of Variables

[19] The example and most of the discussion focus on a change of variables [Gurtin and MacCamy, 1974; Deleersnijder et al., 2001; Delhez et al., 2002; Gomez and Wilson, 2010] because of its intuitive description of the evolution of ADs, relatively straightforward implementation, and novel application to hydrology. The change of variables, which is classical in the conversion of the ADE to a dispersion equation [e.g., Charbeneau, 2000, p. 369], is inspired by the advective nature of equation ((9a)) and its aging term. At any location  $\mathbf{x}$  and time  $t$ , the input time, or first time of appearance into the system, for molecules of age  $\tau$  is  $\eta = t - \tau$ . Let  $\alpha(\mathbf{x}, t, \eta) = \rho(\mathbf{x}, t, t - \eta)$ , then using chain rules we find that

$$\frac{\partial\rho}{\partial t} = \frac{\partial\alpha}{\partial t} + \frac{\partial\alpha}{\partial\eta}, \quad (12a)$$

$$\frac{\partial\rho}{\partial\tau} = -\frac{\partial\alpha}{\partial\eta}. \quad (12b)$$

[20] Substituting these expressions in equations (9) leads to a new mathematical statement, given in equations (13), in terms of  $\alpha(\mathbf{x}, t, \eta)$ . The new PDE does not have derivatives with respect to input time  $\eta$ , but it does have initial and boundary conditions that depend on  $\eta$ . In other words, for a particular point in the spatial domain, the time-age domain is mapped into a time-input time domain (see Figure 1b). In this case, a different problem, with different initial and boundary conditions, is solved for each value of  $\eta$ . Also, a similar mathematical statement is obtained for the cumulative age distribution  $R$ , where the Dirac delta function is replaced by a Heaviside function, and the initial conditions are integrated over the age domain. Notice the similarities between equations (13) and the forward boundary value problem used to describe the AD under steady flow conditions in the generalized reservoir theory (GRT) [see Cornaton and Perrochet, 2006a, equation (2)]. Even though the mathematical statements are analogous, the one for the GRT has some key differences: (i) the variable  $t$  refers to age not time, (ii) flow is time invariant, (iii) the initial condition is zero everywhere within the system, and (iv) the impulse representing the input of new water only occurs at  $t = 0$ .

$$\frac{\partial(\theta\alpha)}{\partial t} + \mathcal{G}(\alpha) = 0, \quad (13a)$$

$$\alpha(\mathbf{x}, t, \eta) = \delta(t - \eta) \quad \text{on } \partial\Omega_1, \quad (13b)$$

$$\mathbf{n} \cdot (\theta\mathbf{D}\nabla\alpha) = 0 \quad \text{on } \partial\Omega_2, \quad (13c)$$

$$\mathbf{n} \cdot (\mathbf{v}\theta\alpha - \theta\mathbf{D}\nabla\alpha) = 0 \quad \text{on} \quad \partial\Omega_3, \quad (13d)$$

$$\alpha(\mathbf{x}, t = t_0, \eta) = \rho_0(\mathbf{x}, t_0 - \eta). \quad (13e)$$

[21] Figure 1b shows some key characteristics (lines with constant  $\eta$ ) in the time-age domain for a particular location  $\mathbf{x}$ . Information is independently transported along these characteristics. Input time values in the interval  $\eta \in [-\infty, t_0]$  refer to the problem with initial conditions given by the initial AD (see equation (13e)). A transport problem is solved to reconstruct the AD along a characteristic  $\eta$  at every point in the domain, using the previously estimated flow field and an initial condition given by the initial AD. Then, at a particular location, the AD at some time  $t'$  is the result of contributions from both the initial distributions ( $\rho_0(\mathbf{x}, \tau)$ ) everywhere in the domain (dark gray area in Figure 1b) and posterior inputs of water through the boundaries or internal sources (clear gray area in Figure 1b). It is worth noting that as time progresses ( $t' \rightarrow \infty$ ) the effect of the initial AD vanishes, leading the system to a new dynamic equilibrium state which only depends on the input of new water. In general,  $\rho_0(\mathbf{x}, \tau)$  is unknown. Then, an initial guess is used and the system modeled in spin-up mode until a dynamic equilibrium is reached. If we are interested in the effects that changes in the hydrologic forcing (e.g., climate change) have on the AD, the dynamic equilibrium becomes the new initial condition and contributes to the further evolution of the ADs. On the other hand, the mathematical statement (equations (13)) simplifies for  $\eta > t_0$ , since  $\rho_0(\mathbf{x}, t_0 - \eta) = 0$ . In this case, the system is forced by instantaneous pulses of new water entering the system along the boundaries at different input times  $\eta$  (see clear gray area in Figure 1b and equations (13b)–(13e)).

[22] The statement in equations (13) can be solved for several discrete values of  $\eta$ , then those results interpolated to find solutions for other values to get the full distribution (not shown). Instead, we discretize the AD to conserve mass and explore in detail the ages of interest. This involves two approximations. First, we lump the AD within any discretized interval. Second, we truncate the AD by neglecting inputs on the ends. A nonuniform discretization of  $\eta$  is used, where the interval  $[\eta_{\min}, \eta_{\max}]$  is split into  $k$  subintervals, leading to bins bounded by  $\eta_i = \eta_{i-1} + \Delta\eta_i$ , where  $i = 1, 2, \dots, k$ ,  $\eta_0 = \eta_{\min}$  and  $\eta_k = \eta_{\max}$ . For each bin the normalized age density is defined as

$$\beta_i(\mathbf{x}, t) = \int_{\eta_{i-1}}^{\eta_i} \alpha(\mathbf{x}, t, \xi) d\xi. \quad (14)$$

[23] Notice that  $\alpha$  and  $\rho$  have units of  $[T^{-1}]$ , but  $\beta_i$  is dimensionless. Then, the expressions in the mathematical statement (equations (13)) can be rewritten for each subinterval as

$$\frac{\partial(\theta\beta_i)}{\partial t} + \mathcal{G}(\beta_i) = 0, \quad (15a)$$

$$\beta_i(\mathbf{x}, t) = H(t - \eta_{i-1}) - H(t - \eta_i) \quad \text{on} \quad \partial\Omega_1, \quad (15b)$$

$$\mathbf{n} \cdot (\theta\mathbf{D}\nabla\beta_i) = 0 \quad \text{on} \quad \partial\Omega_2, \quad (15c)$$

$$\mathbf{n} \cdot (\mathbf{v}\theta\beta_i - \theta\mathbf{D}\nabla\beta_i) = 0 \quad \text{on} \quad \partial\Omega_3, \quad (15d)$$

$$\beta_i(\mathbf{x}, t = t_0) = \int_{-\eta_i}^{-\eta_{i-1}} \rho_0(\mathbf{x}, t_0 - \xi) d\xi. \quad (15e)$$

[24] From the definition of  $\rho$ , we know that for any location  $\mathbf{x}$  at a time  $t$  the AD satisfies  $\int_0^\infty \rho(\mathbf{x}, t, \xi) d\xi = \int_{-\infty}^t \alpha(\mathbf{x}, t, \xi) d\xi = 1$ . This means that the integration along any horizontal trace of the time-age domain of Figure 1b should be unity. So, at a time  $t$ , the cumulative contribution of  $\rho$  from the ages not explored due to truncation (intervals  $\tau \in [0, t - \eta_{\max}] \cup [t - \eta_{\min}, \infty]$ ) can be estimated by using the following expression:

$$\beta_l(\mathbf{x}, t) + \sum_{i=1}^k \beta_i(\mathbf{x}, t) + \beta_r(\mathbf{x}, t) = 1, \quad (16)$$

where  $\beta_l(\mathbf{x}, t) = \int_{\eta_{\max}}^t \alpha(\mathbf{x}, t, \xi) d\xi = \int_0^{t-\eta_{\max}} \rho(\mathbf{x}, t, \xi) d\xi$  and  $\beta_r(\mathbf{x}, t) = \int_{-\infty}^{\eta_{\min}} \alpha(\mathbf{x}, t, \xi) d\xi = \int_{t-\eta_{\min}}^\infty \rho(\mathbf{x}, t, \xi) d\xi$  correspond to the truncated left ( $[0, t - \eta_{\max}]$ ) and right ( $[t - \eta_{\min}, \infty]$ ) sides of the explored domain, respectively. The effect of the initial AD vanishes for a long enough time. Moreover, for  $\eta_{\max} = t$ , the time of interest, the term  $\beta_l$  in equation (16) disappears, leaving us with an expression to estimate the cumulative contribution of the truncated ages

$$\beta_r(\mathbf{x}, t) = \int_{t-\eta_{\min}}^t \rho(\mathbf{x}, t, \xi) d\xi = 1 - \sum_{i=1}^k \beta_i(\mathbf{x}, t), \quad (17)$$

which is used for error analysis.

[25] Finally, the flux-weighted average of the AD over the outflow boundary  $\partial\Omega_2$  is calculated as

$$\rho_{\text{out}}(t, \tau) = \frac{\int_{\partial\Omega_2} (\mathbf{v}\theta\rho - \theta\mathbf{D}\nabla\rho) \cdot \mathbf{ndx}}{\int_{\partial\Omega_2} \theta\mathbf{v} \cdot \mathbf{ndx}}. \quad (18)$$

[26] We use this in the example.

### 2.1.2. Laplace Transforms

[27] The Laplace transform in the age domain of a function  $f(\mathbf{x}, t, \tau)$  is given by

$$\mathcal{Q}[f(\mathbf{x}, t, \tau)] = \bar{f}(\mathbf{x}, t, p) = \int_0^\infty f(\mathbf{x}, t, \tau) e^{-p\tau} d\tau, \quad (19)$$

where  $\mathcal{Q}$  is the Laplace operator with complex valued variable  $p$ . Then, the new mathematical statement, after applying the Laplace transform to expressions (9), is

$$\frac{\partial(\theta\bar{\rho})}{\partial t} + \mathcal{G}(\bar{\rho}) + \theta p\bar{\rho} = 0, \quad (20a)$$

$$\bar{\rho}(\mathbf{x}, t, p) = 1 \quad \text{on} \quad \partial\Omega_1, \quad (20b)$$

$$\mathbf{n} \cdot (\theta\mathbf{D}\nabla\bar{\rho}) = 0 \quad \text{on} \quad \partial\Omega_2, \quad (20c)$$

$$\mathbf{n} \cdot (\mathbf{v}\theta\bar{\rho} - \theta\mathbf{D}\nabla\bar{\rho}) = 0 \quad \text{on} \quad \partial\Omega_3, \quad (20d)$$

$$\bar{\rho}(\mathbf{x}, t = t_0, p) = \bar{\rho}_0(\mathbf{x}, p). \quad (20e)$$

[28] The mathematical statement (equations (20)) changes as a function of  $p$ . For each  $p$  value we have an

independent problem, which allows us to reconstruct  $\bar{\rho}$  using an approach similar to that used for equations (13). Applying the Laplace transform to equation (18), we obtain

$$\bar{\rho}_{\text{out}}(t, p) = \frac{\int_{\partial\Omega_2} (\mathbf{v}\theta\bar{\rho} - \theta\mathbf{D}\nabla\bar{\rho}) \cdot \mathbf{ndx}}{\int_{\partial\Omega_2} \theta\mathbf{v} \cdot \mathbf{ndx}}. \quad (21)$$

[29] After inversion, this expression gives  $\rho_{\text{out}}(t, \tau)$ , the AD on outflow boundaries. *Cornaton* [2012] recently introduced a similar Laplace algorithm for solving the AD problem under time-varying flow regimes.

[30] *Sudicky* [1989] presents a comprehensive description of the solution of the ADE in the Laplace domain and posterior inversion to obtain a time-continuous solution. Solving the problem in the Laplace domain allows us the use of coarser grids without introducing numerical dispersion due to the smoothness of the solution [*Sudicky*, 1989]. Given the damping effect of the kernel in the Laplace operator, a small interval in  $p$  maps into a large interval in the age domain, decreasing the computational burden. *Boupha et al.* [2004] explores the solution of the ADE using Laplace transforms and inverting with the de Hoog algorithm [*de Hoog et al.*, 1982]. This routine can be easily modified to our purposes with the code *invlap.m* implemented by K. J. Hollenbeck (MATLAB customer-contributed code available at [www.mathworks.com](http://www.mathworks.com)), which is a matlab function for numerical inversion of Laplace transforms by the de Hoog algorithm.

### 2.1.3. Modification of Standard Transport Codes

[31] As pointed out by *Ginn* [1999] and *Woolfenden and Ginn* [2009] for problems in one and two spatial dimensions, equation (9a) can be seen as the traditional higher dimensional ADE with an additional spatial dimension replaced by age ( $\tau$ ). In that case, the pore velocity in the age dimension is one, and the dispersion tensor is modified to ignore dispersion in the age dimension. For example, for a 3-D computer code applied to a 2-D spatial domain ( $x, y$ ) in which the  $z$  coordinate is replaced by age we have

$$\mathbf{v}(\mathbf{x}, t) = (v_x, v_y, 1) \quad (22)$$

$$\mathbf{D} = \begin{pmatrix} D_{xx} & D_{xy} & 0 \\ D_{yx} & D_{yy} & 0 \\ 0 & 0 & 0 \end{pmatrix}, \quad (23)$$

where  $v_x$  and  $v_y$  are estimated with a flow code, and the nonzero terms in the dispersion tensor are estimated with equation (2). Two issues should be considered in this case when conventional numerical solution methods are employed: (i) the infinite age dimension is represented by a finite spatial domain, and (ii) the numerical solution of the ADE with zero dispersion in one direction is challenging. The mathematical statement (equations (9)) represents an initial value problem in both time and age, which models the evolution of the initial AD at every location in the domain. At any location and time (with the exception of source areas), the AD satisfies  $\rho(\mathbf{x}, t, \tau = 0) = 0$  and  $\rho(\mathbf{x}, t, \tau \rightarrow \infty) \rightarrow 0$ , simultaneously. However, for a finite age domain  $[0, \tau_{\text{max}}]$ , the constraint at  $\tau_{\text{max}}$  is unknown,

and therefore, the age domain must be large enough to prevent the influence of this large age ‘‘boundary condition’’ [*Woolfenden and Ginn*, 2009]. The question becomes how large is large enough? In this regard, the adequacy of the domain’s size can be tested by solving the problem with two different constraints at  $\tau_{\text{max}}$ , a Neumann type (no age gradient,  $\partial\rho/\partial\tau = 0$ ) and a Dirichlet type (prescribed age,  $\rho = 0$ ). If they lead to essentially the same result, the size of the age domain is adequate. Or, alternatively, the problem can be solved with prescribed age ( $\rho = 0$ ) boundary conditions at both ends but for different domain sizes  $\tau_{\text{max}}$ . An adequate and parsimonious size is reached when the solution becomes insensitive to changes in  $\tau_{\text{max}}$ . Finally, the selection of the computer code and transport algorithm plays a key role, since these can lead to excessive numerical dispersion and/or oscillations and possibly invalidate the approach.

### 3. Example: Topography-Driven Flow

[32] Water flow in RGSs and HZs is strongly influenced by the spatial distribution of hydraulic head along the top boundary. This boundary is affected by weather and climatic variability, leading to an inherited dynamic behavior in the subsurface flow field. For example, regional groundwater flow determines the large-scale interactions between groundwater and surface water known as large-scale exchange [*Sophocleous*, 2002], in which analysis has been traditionally based on the concept of hierarchical flow systems introduced by *Tóth* [1962]. This conceptual model is a good approximation for more humid areas with considerable recharge where the groundwater table, the top boundary, can be idealized as a subdued replica of the ground surface topography [*Tóth*, 1962, 1963; *Freeze and Witherspoon*, 1966, 1967; *Tóth*, 2009]. The traditional Tóthian conceptual model assumes that the water-table position is known and represented by a sinusoidal signal superimposed on a linear trend. In a similar fashion, stream-channel slope discontinuities (e.g., ripples, dunes, and riffle-pool sequences) create a spatially variable head distribution at the water-sediment interface, the top boundary of the sediments, that induces short-scale HZ exchange and can also be idealized as a sinusoidal signal superimposed on a linear trend [*Fehlman*, 1985; *Harvey and Bencala*, 1993; *Elliott and Brooks*, 1997a, 1997b; *Boano et al.*, 2010]. In both cases, the hierarchical flow conceptualization is both useful and accurate.

[33] In this section, we use a Tóthian-like model to illustrate the importance of flow dynamics in ADs for RGSs and HZs. The primary difference is one of the scales in both space and time. RGSs have spatial scales of kilometers or more, while HZs have scales of less than a meter to tens of meters. RGSs have temporal scales of months to millennia, while HZs have scales of minutes to weeks. We explore different scales by presenting our results in dimensionless form. We start with the flow model for RGSs and then extend those results to HZs.

[34] The transient regional groundwater flow system is represented by a cross-sectional Tóthian-like domain [*Tóth*, 1962, 1963], filled with a heterogeneous and anisotropic porous media (see Figure 2a). The system is bounded by the water table at the top and impermeable boundaries on

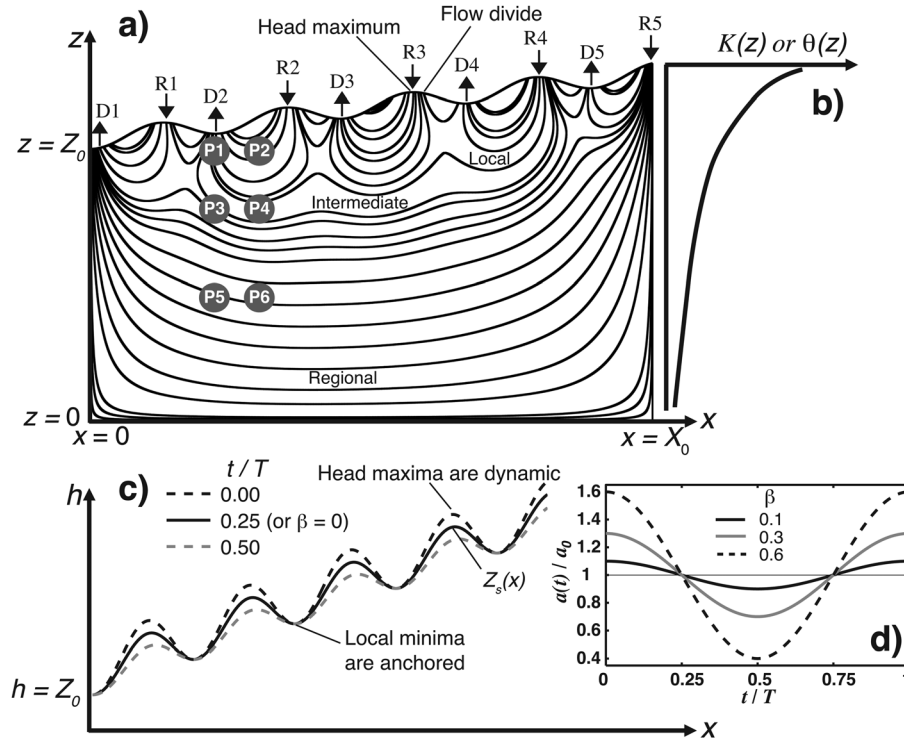


**Figure 2.** Schematic representation of (a) the topography-driven flow system with a snap shot of a typical flow field ( $t/T = 0.25$ ,  $\beta = 0.3$ ), (b) the typical depth dependence of porosity or hydraulic conductivity, (c) the spatial pattern of head along the top boundary for three different times ( $t/T = 0, 0.25$ , and  $0.50$ ), and (d) the time variation of water table amplitude for three different conditions representing intensity of the variation ( $\beta$ ). Points P1–P6 are located in the local, intermediate, and regional flow paths observed under steady flow for the system with aspect ratio  $X_0/Z_0 = 20$ . These observation points are located under the discharge zone D2 and one of its corresponding hillslopes, and they are used to illustrate the changes in ADs in section 4.3.

the other three sides. The porous media flow is modeled by Darcy's law and the continuity equation for incompressible flow in a nondeformable media (groundwater flow equation), ignoring the effects of specific storage:

$$\frac{\partial}{\partial x} \left( K_x(x, z) \frac{\partial h}{\partial x} \right) + \frac{\partial}{\partial z} \left( K_z(x, z) \frac{\partial h}{\partial z} \right) = 0, \quad \begin{aligned} 0 < x < X_0, \\ 0 < z < Z_s, \end{aligned} \quad (24)$$

where  $h(\mathbf{x}, t)$  is hydraulic head,  $\mathbf{x} = (x, z)$  is the spatial location vector, and  $K_x(x, z)$  and  $K_z(x, z)$  are the horizontal and vertical hydraulic conductivities, respectively. The temporal dependence of the hydraulic head arises from the time-dependent head prescribed at the top of the domain (see equation (26)) and is described in more detail in the following paragraphs. We performed simulations with and without specific storage for the range of investigated parameters (not shown) and found that neglecting the specific storage has little impact on the hydraulic head and flow fields and therefore does not change the results presented. The specific discharge is derived from Darcy's law as  $\mathbf{q} = \theta(x, z)\mathbf{v} = -[K_x(x, z)\partial h/\partial x, K_z(x, z)\partial h/\partial z]$ . Hydraulic conductivity and porosity are assumed to decrease expo-

entially with depth (Figure 2b) as [Ingebritsen and Manning, 1999; Jiang et al., 2009, 2010a]

$$\begin{aligned} K_x(x, z) &= K_{0,x} \exp[-A(Z_s(x) - z)] \\ K_z(x, z) &= K_{0,z} \exp[-A(Z_s(x) - z)] \\ \theta(x, z) &= \theta_0 \exp[-(A/n)(Z_s(x) - z)], \end{aligned} \quad (25)$$

where the horizontal and vertical hydraulic conductivity and porosity at the top boundary are given, respectively, by  $K_{0,x}$ ,  $K_{0,z}$ , and  $\theta_0$ ;  $A$  is the rate of exponential decrease;  $n$  is a medium- and process-dependent coefficient;  $X_0$  is the aquifer length; and  $Z_s(x)$  is the elevation of the top boundary above the aquifer base.  $Z_s(x)$  is determined from the thickness of the aquifer ( $Z_0$ ) below the downgradient discharge area (at  $x=0$ ), the upper boundary head gradient ( $m$ ), the amplitude of the local, topographically controlled, spatial variations ( $a_0$ ) of head along the upper boundary, and the wavelength of those spatial variations ( $\lambda$ ).

[35] No-flow,  $\mathbf{n} \cdot \mathbf{q} = 0$  where  $\mathbf{n}$  is an outward normal vector, boundary conditions are used for the bottom and sides of the domain ( $\partial\Omega_3$  for age modeling). At the top of the domain, boundary conditions are prescribed to resemble a transient forcing by imposing the hydraulic head distribution as a time-varying Dirichlet boundary, which implies fluctuating zones of both inflow ( $\partial\Omega_1$ ) and outflow ( $\partial\Omega_2$ ).

The following harmonic head distribution is used for this purpose (see Figures 2c and 2d):

$$h(x, z = Z_s(x), t) = Z_0 + mx + a(t) \sin\left(\frac{2\pi}{\lambda}x + \delta_x(t)\right) - \delta_z(t),$$

$$\text{with } a(t) = a_0 \left[1 + \beta \cos\left(\frac{2\pi}{T}t\right)\right], \quad (26)$$

where  $a(t)$  is the time-varying amplitude of the head (controlled by the parameter  $\beta$ ),  $T$  is the period, the phase lag  $\delta_x(t)$  is the solution to the transcendental equation

$$m + \frac{2\pi a(t)}{\lambda} \sin(\delta_x(t)) = 0, \quad (27)$$

and the vertical displacement  $\delta_z(t)$  is defined as

$$\delta_z(t) = a(t) \sin(\delta_x(t)). \quad (28)$$

[36] Both the phase lag and the vertical displacement lead to a fluctuating head with two characteristics commonly found for the water table in natural regional groundwater flow systems: (i) the minima are anchored (i.e., the streams are anchored), while the amplitude fluctuates, and (ii) maxima and nearby groundwater divides are dynamic in both elevation and location. This type of behavior in the water table mimics the response to temporal variability in recharge rates for a watershed with perennial streams. In this case, increase or reduction of recharge can be caused by seasonal variability or longer dry-wet transitions caused by atmospheric drivers such as the El Niño-Southern Oscillation (ENSO) or the Pacific Decadal Oscillation (PDO).

[37] Although the hydraulic head along the top boundary fluctuates, we fix its geometric elevation, avoiding the need for an adaptive gridding scheme and ignoring the effects of specific yield. This is a good approximation as long as water-table fluctuations in RGSs are small compared to the size of the domain (sufficiently small  $\beta$  or  $a_0$ ; not shown). In this case the system responds fast relative to the period of the water-table fluctuations and is essentially incompressible and nondeformable. This assumption, however, is invalid if a point source or sink (e.g., a well) is introduced. *Tóth* [1962, 1963] originally used a rectangular domain, with a constant elevation for the top boundary. Instead, we fix the elevation of the top boundary to correspond to the water-table elevation (equation (26)) with  $\beta = 0$  or  $t = T/4$  (see Figure 2c), or

$$Z_s(x) = Z_0 + mx + a_0 \sin\left(\frac{2\pi}{\lambda}x + \delta_x\left(\frac{T}{4}\right)\right) - \delta_z\left(\frac{T}{4}\right). \quad (29)$$

[38] This is also the hydraulic head used at the top boundary for steady-state runs. In short, while the head on the upper boundary fluctuates (equation (26)), its geometric location (equation (29)) does not.

[39] Notice that for a particular time, equation (26) is analogous to the sinusoidal forcing used in the classical *Tóthian* domain [e.g., *Tóth*, 1962]; however, to anchor the local minima of the harmonic function (i.e., the streams in the case of a RGS), an amplitude-dependent phase lag (equation (27)) and vertical displacement (equation (28)) are introduced. The time-varying water-table head (equation (26))

fluctuates at a frequency  $2\pi T^{-1}$ , and the factor  $\beta$  reflects the intensity of these temporal fluctuations. Imposing this Dirichlet boundary condition at the top of the domain results in a harmonic behavior of the recharge and discharge rates and locations and a temporal evolution of the flow field.

[40] We can use the same model to approximate HZs, although three aspects of our conceptual model require comment for the HZ application. First, in equation (26) the amplitude  $a(t)$  of the boundary head fluctuates over time, but not its slope  $m$ . For HZs this is appropriate for head fluctuations induced by slowly varying mean uniform channel flow. Second, the elevation of the top boundary (equation (29)) has the same pattern as the topography in RGSs, but the topography of the water-sediment interface and the head distribution along that interface are somewhat different (see *Cardenas and Wilson*, 2007a, Figure 4; *Cardenas and Wilson*, 2007b, Figure 3). HZ models that use a sinusoidal signal superimposed on a linear trend [*Fehlman*, 1985; *Harvey and Bencala*, 1993; *Elliott and Brooks*, 1997a, 1997b; *Boano et al.*, 2010] avoid this issue by assuming a rectangular domain, just as *Tóth* originally did for RGSs. In any event, the geometric amplitude of the top elevation of our model ( $a_0$ ) is small enough that it has only a second-order impact (not shown), allowing us to interpret the results to apply to HZs as well as RGSs. Third, there is no specific yield at the upper boundary of a HZ, therefore neglecting it is not an approximation. When referring to recharge and discharge in the example below, the HZ equivalents are downwelling and upwelling from/to the stream channel.

[41] The flow field is characterized by nested flow paths (see Figure 2a), with patterns that change over time. A two-fold approach is used to explore how the flow field and groundwater age change across the broad suite of parameters that characterize both RGSs and HZs. Given the considerable computational efforts required for a full sensitivity analysis, particularly to model the full ADs, we first explore the parameter space for the flow field and first moment of the AD ( $a_1(t)$ ), and then, based on this analysis, some of the most interesting scenarios are modeled for full ADs  $\rho$  and  $R$ .

[42] Table 1 presents the dimensionless ratios used for the analysis. The values explored for these ratios are based on previous works that use a similar conceptual model [e.g., *Tóth*, 1962, 1963, 2009; *Ophori and Toth*, 1990; *Cardenas*, 2007; *Gleeson and Manning*, 2008; *Jiang et al.*, 2009, 2010b; *Cardenas and Jiang*, 2010], and they are relevant for either RGSs or HZs. The domain geometry is defined by the ratios  $X_0/\lambda$  and  $X_0/Z_0$ , where the first is kept constant and the second (aspect ratio of the domain) is varied to mimic a thin domain (e.g., aquifers commonly found in nature) and a thick domain (e.g., HZs). The system is characterized by several ratios; however, the surface porosity ( $\theta_0$ ), porosity-depth decay factor ( $n$ ), and the local anisotropy in hydraulic conductivity ( $K_{0,z}/K_{0,x}$ ) are kept constant. The product  $A\lambda$  represents the depth-decay rate for hydraulic conductivity (e.g.,  $A\lambda = 4$  means that the hydraulic conductivity has decayed by a factor  $e^{-4}$  at a depth  $\lambda$ ). The scale dependence of dispersion has been well documented (see *Gelhar et al.*, 1992, Figure 1; *SchulzeMakuch*, 2005]; however, most mathematical models for solute

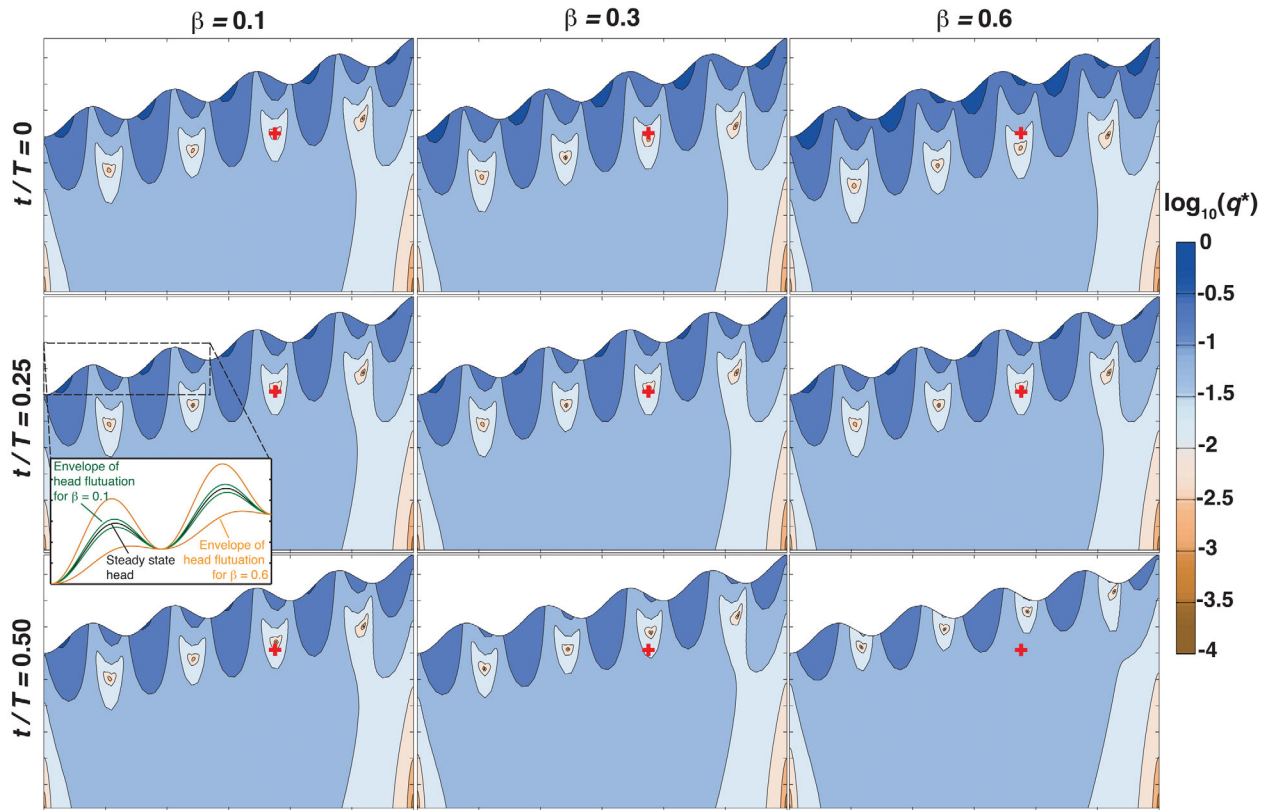


**Figure 3.** Snapshots at (rows) different times over the forcing's period ( $t/T = 0, 0.25,$  and  $0.50$ ) of the magnitude of the dimensionless Darcy flux ( $|\mathbf{q}^*| = |\mathbf{q}|/K_{0,x}$ ) for (columns) different fluctuation intensities ( $\beta = 0.1, 0.3,$  and  $0.6$ ). The color bar represents the magnitude of the dimensionless flux ( $X_0/Z_0 = 20, A\lambda = 4$ .) Red crosses mark the location of the same stagnation point at  $t/T = 0$  and  $\beta = 0.1$  for all the snapshots and are for reference. Vertical axes are exaggerated for visualization purposes.

transport, like the ADE used in this study, ignore this aspect and assume fixed values of dispersivity. Our analysis explores two values of longitudinal dispersivity, represented by the ratio  $\lambda/\alpha_l$ . The smaller ratio represents the upper limit of dispersivity found in natural systems, while the larger ratio represents an intermediate value of dispersivity (lower values of dispersivity are not used to avoid the higher discretization required by the numerical solution method and possible numerical dispersion or instabilities). Similarly, it has been observed that the ratio of transversal and longitudinal dispersivities varies over three orders of magnitude [see *Gelhar et al.*, 1992, Table 1 and Figure 6]. We explore two ratios, where the lower one represents commonly found values and the larger the upper limit found in natural systems [see *Gelhar et al.*, 1992, Figure 6]. The exchange between flow tubes increases with this ratio, and therefore, it is of particular interest for age modeling. Lower values of this ratio are not explored due to computational demand and numerical issues as explained before.

[43] The intensity of temporal fluctuations in the forcing is characterized by the parameter  $\beta$ . In this case, three values were used to represent this intensity, where the smaller value is representative of most regional aquifers and the larger value of HZs, where strong changes in river stage and discharge generate oscillations of this magnitude and larger. The ratio of the forcing time scale  $T$  and a character-

istic advective time scale of the system ( $(\lambda\theta_0)/(K_{0,x}m)$ ) was used to characterize the expected response of the flow field to a given frequency of fluctuations (the advective time scale represents the advective time for an equivalent porous media with porosity  $\theta_0$ , hydraulic conductivity  $K_{0,x}$ , and size  $\lambda$  exposed to a hydraulic gradient  $m$ ). Even though this characteristic time scale does not describe exactly the response of the system's ADs to transient forcing, it can be used to describe situations where these fluctuations are expected to be unimportant. For example, if the ratio is much larger than one, the system is quasi-steady, and these fluctuations are ignored. On the other hand, if the ratio is much lower than one, the forcing fluctuations are filtered out by the system. Our simulations focus on realistic time scales that lead to ratios close to one; however, future work should focus on further exploring the important forcing time scales for natural hydrologic systems. Decadal fluctuations of climate, which affect recharge at the regional scale, are an example of the type of temporal fluctuation with a ratio close to one for most RGS. These decadal oscillations ( $T = 10$  years) associated with climatic signals such as ENSO and the PDO have been shown to have important effects on regional aquifer recharge and water-table fluctuations in the western United States [e.g., *Alley et al.*, 2002; *Phillips et al.*, 2004; *Anderson and Emanuel*, 2008; *Barco et al.*, 2010]. In a similar fashion, flood events at the scales

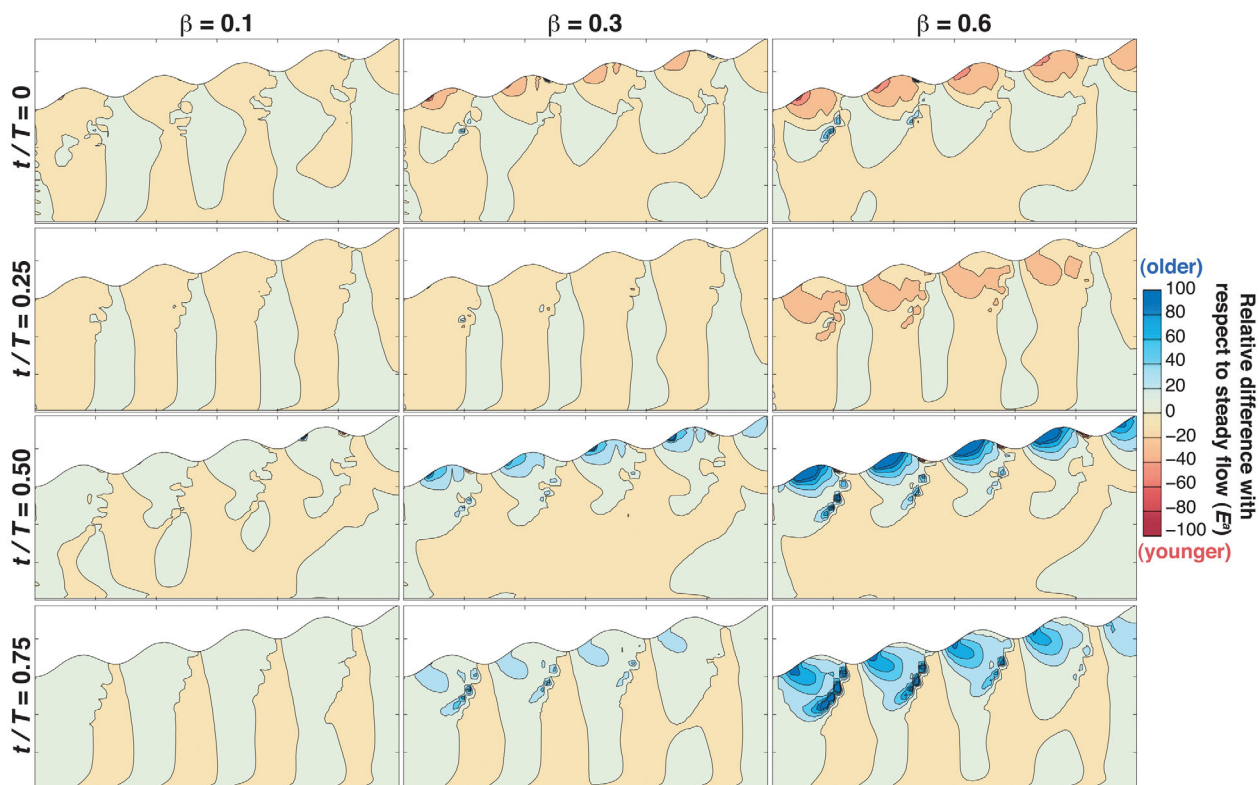


**Figure 4.** Snapshots at (rows) different times ( $t/T = 0, 0.25, 0.50,$  and  $0.75$ ) of the relative differences (equation (30)) of transient flow mean ages with respect to the steady flow mean ages ( $E^s$ ) for (columns) different fluctuation intensities ( $\beta = 0.1, 0.3,$  and  $0.6$ ). The relative change is calculated with respect to the steady flow mean age ( $a_1^s$ ), after dynamic equilibrium is reached, for different times during the cycle. Hotter colors are younger. ( $X_0/Z_0 = 20, A\lambda = 4, \lambda/\alpha_L = 133.3, \alpha_T/\alpha_L = 0.1$ .) Vertical axes are exaggerated for visualization purposes.

of hours to days present a ratio close to one for the case of HZs controlled by channel slope discontinuities [e.g., *Boano et al., 2010*].

[44] Finally, the governing equations (24) and (15a) are sequentially solved with the finite-element method implemented in COMSOL Multiphysics. A typical grid has 15,000 triangular elements with closer grid spacing at shallower depths. We verified that the solutions are mesh independent.

**Table 1.** Parameters Used for Sensitivity Analysis

Type of Property	Dimensionless Ratio	Value
Domain geometry	$X_0/\lambda$	4.5
	$X_0/Z_0$	20 and 10
System properties	$\theta_0$	0.3
	$n$	2
	$A\lambda$	0, 4, and 14
	$\lambda/\alpha_L$	13.3 and 133.3
	$\alpha_T/\alpha_L$	0.1 and 0.5
Forcing dynamics	$K_{0,z}/K_{0,x}$	0.1
	$\beta$	0.1, 0.3, 0.6
	$mX_0/a_0$	7.5
	$m$	0.025
	$(TK_{0,x}m)/(\lambda\theta_0)$	0.31

## 4. Results

### 4.1. Flow Field

[45] The forcing used in this model is harmonic, in both space and time. Spatial variations in top head boundary (slope and sine component in equation (26)) result in a hierarchical flow field with time-varying local, intermediate, and regional flow paths (see Figure 2a). Although this conceptual model is an analog for both regional flow systems (RGSs) and HZs, without loss of generality, we use the terminology traditionally employed for RGS, where flow paths associated with short-scale, intermediate-scale, and large-scale interactions are referred as local, intermediate, and regional flow paths. The flow field is characterized by a sequence of alternating recharge ( $\partial\Omega_1$ ) and discharge ( $\partial\Omega_2$ ) zones (in HZs, downwelling and upwelling zones) that expand and contract with time. Local circulation systems present high pore velocities, compared with other parts of the system, and therefore a continuous and highly dynamic replenishment with younger waters. On the other hand, regional flow paths tend to have small pore velocities and older waters. In this regard, notice that the flow in deeper portions of the system is less sensitive to head boundary fluctuations and that the shape and penetration of the local systems are mostly controlled by the head boundary amplitude ( $a(t)$ ) and wavelength ( $\lambda$ ) and the spatial variations in hydraulic conductivity.

[46] The dynamic nature of the forcing causes recharge and discharge zones, and flow hinge points, divides, and stagnation zones to move. Figure 3 presents typical snapshots for the spatial distribution of the magnitude of dimensionless Darcy flux ( $\mathbf{q}^*(\mathbf{x}, t) = \mathbf{q}(\mathbf{x}, t)/K_{0,x}$ ) for three different times ( $t/T=0, 0.25, 0.50$ ; rows) and fluctuation intensities ( $\beta=0.1, 0.3, 0.6$ ; columns). Local flow paths are characterized by high pore velocities, reaching their maximum and minimum magnitudes at the beginning ( $t/T=0$  or  $t/T=1$ ) and middle ( $t/T=0.5$ ) of a period, respectively. These flow paths originate in the recharge zones around the local maxima of the head boundary (i.e., near divides) and converge toward an adjacent discharge zone around the local minima of the head boundary (Figure 2a). Notice that some of the flow paths converge toward discharge zones downgradient of the nearest local minimum, giving rise to intermediate and regional flow paths. Similarly, a discharge zone can receive contributions from intermediate and regional flow paths. The proportion of mass delivered by these longer flow paths is a function of the forcing and system properties and changes with time. The importance of contributions from local flow paths is highlighted when flux is integrated across individual discharge zones, which is equivalent to averaging over several flow paths. Discharge-zone flux is highly sensitive to increases in the strength of the fluctuations  $\beta$  (e.g., flux in discharge zone D1 varies from  $\pm 5\%$  with  $\beta = 0.1$  to  $\pm 40\%$  with  $\beta = 0.6$ ), and this sensitivity increases with the contribution of local flow paths (not shown).

[47] With this in mind, we can associate a left and right slope to each local minima along the top head boundary shown in Figures 2a and 2c. Relative to the regional system these slopes are, respectively, downgradient and upgradient of the local minima. They start at the local minima and rise on each side to the nearest local maxima, containing a flow hinge point in between. The slopes are analogous to the head observed in a hillslope draining to a stream for a RGS or the trough (left) and lee (right) slopes for a channel slope discontinuity inducing hyporheic exchange (e.g., dune, ripple, or pool-ripple). The nested system of flow paths originating on the right (upgradient) slope has a larger flow contribution to its local discharge zone, presents higher pore velocities, and penetrates deeper into the system when compared with the left slope (Figures 2a and 3). All left (downgradient) slopes have a low-velocity or stagnation zone (see hotter colors in Figure 3) consistently located underneath. These stagnation zones stretch, contract, and move up and down over time as the amplitude of the forcing changes, playing a key role in the evolution of ADs, since their position is associated with acceleration, deceleration, and direction changes for moving water. For large fluctuation intensities  $\beta$ , the stagnation zone moves very close to the surface, and the flow contribution from the left slope almost vanishes (see Figure 3;  $t/T = 0.5, \beta = 0.6$ ).

[48] Consider each of the three specific times illustrated by a row in Figure 3. The center row,  $t/T = 0.25$ , also corresponds to the conditions for the steady-state simulation. Since storage is neglected in our flow model, all three plots on the center row are identical to the steady-state flow field and to each other. The top row,  $t/T = 0.0$ , corresponds to the time that the boundary head is at its temporal highest (Figure 2d). Since the minimum boundary head is anchored

(equation (26)), this means that the largest gradient in the local flow system occurs at this time, while the smallest occurs later in the cycle, at  $t/T = 0.5$ , corresponding to the bottom row. In short, the strongest local flow is associated with  $t/T = 0.0$  and the top row, and the weakest is associated with  $t/T = 0.5$  and the bottom row. What happens as the boundary head amplitude ( $\beta$ ) increases from left to right for the top and bottom rows in Figure 3? The strongest flow becomes larger since the peak boundary head is higher, and the weakest flow becomes even weaker since the peak head is now smaller. As a consequence, as we go from left to right in the first (third) row we see (i) the flushing intensities of the local flow systems increase (decrease), (ii) local flow systems penetrate deeper (shallower), and (iii) the locations of low-velocity and stagnation zones deepen (become more shallow), and their vertical extent increases (decrease). In the third row the stagnation zones also migrate slightly to the right (upgradient) with increasing  $\beta$ .

[49] Intermediate flow paths are best observed in Figure 2a. These flow paths play a fundamental role in the nested flow system and aging of water since they are the active mixing zone between young and old water traveling along local and regional flow paths, respectively. Moreover, intermediate flow paths have the second largest contribution to discharge zones after the local flow paths. Regional flow paths transport the oldest water and, in general, have a small contribution to the discharge zones. Moreover, their behavior is barely affected by the transient forcing, with flow velocity magnitudes and directions that are almost time invariant, leaving mixing due to diffusion and dispersion, enhanced by flow dynamics, as the main mechanism for temporal changes in the AD at these deep locations.

[50] Decay of the hydraulic conductivity counteracts the effects of increasing amplitude of the water-table fluctuations but, at the same time, enhances penetration of the local systems as the depth-decay rate increases (increase of the ratio  $A\lambda$ ; not shown). This is consistent with Jiang *et al.* [2009] who found that the faster the porosity and hydraulic conductivity decay with depth, the larger the contribution of the local flow paths relative to the intermediate and regional flow paths to the discharge zones and the larger the depth of the local flow. Deeper parts of the system present stronger responses to changes in depth-decay rates for porosity and hydraulic conductivity (not shown), given the exponential nature of the model used to mimic the spatial patterns of these parameters. In general, as the depth-decay rate increases, the focus of variability for flow concentrates almost exclusively in the shallower parts of the system, leading to larger portions of the lower domain where the flow is insensitive to temporal fluctuations in the head boundary.

[51] As a consequence of dynamic forcing, every point of the domain is exposed to pore velocities that change direction, accelerating, and decelerating as time progresses. For instance, imagine a water parcel traveling along a fast, local flow path at a certain time. If the flow is steady, this parcel remains in the same flow tube for the rest of its journey unless mixing due to dispersion or diffusion moves it to a different flow tube affecting its aging. Transient flow has a similar mixing effect on a water parcel, but in this case it is induced by fluctuations of the flow paths and is on

a much larger scale. For example, due to these fluctuations a water parcel that was on a fast path can later find itself on a slow path, and later still be back on a fast path. Dynamic flow fields induce mixing which is different to that caused by dispersion or diffusion, but it has a similar effect on ADs. This behavior is most evident in the shallow parts of the system, where, as mentioned before, the flow is more sensitive to water-table fluctuations. There is some previous work focused on the study of apparent transverse dispersion caused by transient fluctuations in groundwater flow [e.g., *Goode and Konikow*, 1990; *Wood and Kavvas*, 1999a, 1999b; *Cirpka and Attinger*, 2003] and its role on biochemical transformations [*Prommer et al.*, 2002; *Schirmer et al.*, 2001]. In general, changes in direction are a dominant factor affecting this mixing effect [*Goode and Konikow*, 1990], and systems with low storativity, like the one used in this example, tend to be more affected since flow responds almost instantly to changes in forcing.

[52] In the following subsections, zones of high sensitivity of the age to transient forcing are closely related to zones of highly variable flow direction, rather than variations in flow magnitude. Our local flow systems are most strongly affected by fluctuations in the forcing, creating dynamic stagnation zones that evolve over time and induce changes in flow direction and magnitude. These changes affect ADs in shallow portions of system and in discharge zones. In contrast, regional flow paths are less responsive to fluctuations in the forcing, leaving dispersion and diffusion as the main transverse mixing process affecting ages in deeper parts of the system.

## 4.2. Mean Ages

[53] The spatial and temporal distributions for the first moment of the AD ( $a_1$ ) are estimated from expressions (11). The first moment is a useful metric to evaluate the influence of transience on ADs and has been used to model the evolution of mean age during a pumping test in real fractured rock aquifers [e.g., *Goode*, 1998, 1999] and hypothetical unconfined and layered aquifer systems stressed by pumping [e.g., *Zinn and Konikow*, 2007a, 2007b]. A typical plot of mean age for steady flow can be found in *Jiang et al.* [2010b, Figure 3]. In the transient case, after a dynamic equilibrium is reached, first moment fields follow a periodic behavior with period  $T$  due to the harmonic nature of the forcing and the system's characteristics. In general, local flow systems are characterized by younger water, evidencing a fast and constant replenishment of recharged water. Older ages are found deeper in the system, influenced by intermediate and regional flow paths, and toward the regional discharge end of the flow field.

### 4.2.1. Spatial Patterns of Mean Age

[54] To measure the importance of flow dynamics on the mean of the AD, fields of the relative difference between the mean age under transient flow at a particular time during the period ( $a_1(\mathbf{x}, t)$ ) and the mean age under steady flow ( $a_1^s(\mathbf{x})$ ) are estimated as

$$E^a(\mathbf{x}, t) = \left[ \frac{a_1(\mathbf{x}, t) - a_1^s(\mathbf{x})}{a_1^s(\mathbf{x})} \right] \times 100. \quad (30)$$

[55] Figure 4 exemplifies the results obtained for the relative differences  $E^a(\mathbf{x}, t)$  from sensitivity analyses with

head boundary fluctuation intensities  $\beta = 0.1, 0.3$ , and  $0.6$ ; it shows plots of  $E^a(\mathbf{x}, t)$  at different times over a period after dynamic equilibrium is reached. Mean ages within local flow systems, especially close to recharge zones, are highly sensitive to flow dynamics, presenting relative differences larger than 50% in absolute value (dark blue and red areas to the left of the local boundary head maxima). Early in the cycle these high-sensitivity zones are associated with relatively young waters (red hot spots in Figure 4,  $t/T = 0, 0.25$ ), since the transient amplitude of the forcing is larger than the amplitude under steady flow. Later in the cycle, as the transient amplitude of the forcing decreases, the high-sensitivity areas become dominated by older relative ages (blue cold spots in Figure 4,  $t/T = 0.50, 0.75$ ). Mean ages in deeper parts of the system are less sensitive to fluctuations in the forcing ( $E^a(\mathbf{x}, t) \rightarrow 0$ ) because perturbations in the flow field, caused by temporal fluctuations in the forcing, vanish with depth and because transverse mixing is usually not strong enough to exchange water between shallow and deep flow paths.

[56] The nested flow paths in this Tóthian-like system have a broad range of characteristic time scales, ranging from short time scales in the local flow system to large time scales in the regional flow system. Under small fluctuations ( $\beta = 0.1$ ), the mean ages change only slightly with time ( $|E^a(\mathbf{x}, t)| < 20\%$ ) at all scales; however, the high-sensitivity zones are still present. For large fluctuations ( $\beta = 0.3, 0.6$ ) the sensitivity dramatically increases, especially in locations with either the highest flow velocities or largest variabilities in flow direction (corresponding to the blue cold spots in Figure 4; also, see Figure 5). Moreover, there is a time lag between the largest amplitudes of the forcing ( $t/T = 0$ ) and the largest differences in the mean ages. Age, unlike the flow field in this model, has memory. This is further illustrated in Figure 4 by the faint presence of cold spots during the periods when the transient forcing amplitude is larger than the steady amplitude ( $t/T = 0$ ), and by the chain of successively older cold spots tracking past stagnation zones that is obvious during periods when the transient forcing amplitude is smaller ( $t/T = 0.50, 0.75$ ).

[57] The right (upgradient) slopes of the local minima, where the largest differences originate, are the focus of the greatest fluctuations of age. The main reason for this behavior is the dynamic nature of the location of head maxima along the top boundary; they (and the flow divides) move from right to left as the amplitude of the forcing increases (see Figure 2c). This in turn decreases the proportion of local flow to the left and increases it to the right. To the right of these high-sensitivity zones, below the next left slope, the chain of blue cold spots ( $t/T = 0.50, 0.75$ ), a sequence of detached zones of high sensitivity, appears deeper in the domain as times progresses (the pattern is periodic). These are zones associated with changes in flow rate and direction, and moving stagnation zones (see Figure 5). Changes in flow direction have a strong effect on ages because water that was originally circulating in a local flow path from a left slope to a minima will change direction and discharge in the next minima downgradient or continue into an intermediate or regional flow path. In particular, changes in the shape and position of stagnation zones lead to large fluctuations in pore velocity direction and

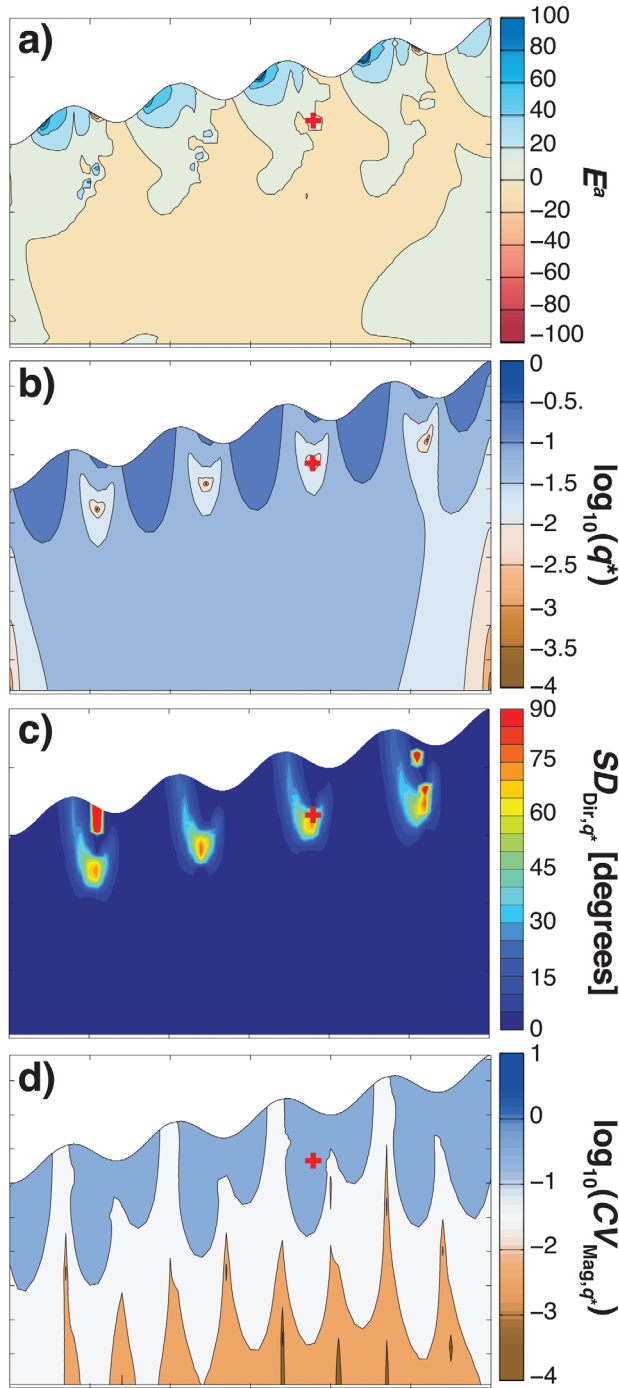


**Figure 5.** Snapshot at  $t/T = 0.50$  of the (a) relative difference of transient flow mean ages with respect to the steady flow mean ages ( $E^a$ ) and (b) dimensionless Darcy flux ( $|\mathbf{q}^*$ ) for fluctuation intensity  $\beta = 0.3$ . (c) Scaled standard deviation for the flow direction ( $SD_{Dir,q^*}/\pi$ ) and (d) coefficient of variation for the flow magnitude ( $CV_{Mag,q^*}$ ) are shown. The red crosses mark the location of one of the high-sensitivity spots observed in (a). This high-sensitivity spot is correlated to the stagnation zones (b) and areas with high variability in flow direction (c). ( $X_0/Z_0 = 20$ ,  $A\lambda = 4$ ,  $\lambda/\alpha_L = 133.3$ ,  $\alpha_T/\alpha_L = 0.1$ .)

magnitude. These effects are responsible for this chain of detached zones of high sensitivity.

[58] Different variables affect the shape and penetration depth of the high-sensitivity zones (dark red or blue); however, the aim of this paper is not to perform a full sensitivity analysis but to point out the potential importance of dynamics on ADs. In this advection dominated system, changing the magnitude of the hydraulic conductivity by multiplying it by a uniform constant across the domain does not affect the pattern of flow or the relative difference fields,  $E^a(\mathbf{x}, t)$ , shown in Figure 4, but it changes the magnitude of the flow velocity and the ages. On the other hand, changing the spatial pattern or anisotropy of hydraulic conductivity has a strong effect on the penetration of the high-sensitivity zones. For example, as the conductivity and porosity decay rate ( $A\lambda$ ) increases, the zones of high sensitivity with younger waters (hot spots in Figure 4) are compressed and limited to shallower areas, while the ones leading to older ages (cold spots in Figure 4) penetrate deeper in the domain (not shown). As the dispersivity ratio  $\alpha_t/\alpha_l$  increases, the cold spots of high sensitivity have smaller values but are wider, effectively spreading the zone of sensitivity (not shown). Similarly, increases in longitudinal dispersivity lead to smoothing of the high-sensitivity areas, redistributing the differences and attenuating the sensitivity. Finally, changes in the period of the temporal fluctuation ( $T$ ) affect the patterns observed for relative difference  $E^a(\mathbf{x}, t)$ , depending on the ratio of the period of fluctuation and the characteristic time scale for transport. The transport time scale used in Table 1,  $(TK_{0,x}m)/(\lambda\theta_0)$ , best represents the response of shallow parts of the system. Small and large values of this ratio correspond to a signal that is not seen or filtered out by the system, respectively. The second of these is the case in the deeper parts of the system. When the ratio is close to one, both time scales are comparable, and the sensitivity to dynamics increases, as we observe in the shallow circulation systems.

[59] Under the premise that the mean age can be used as a proxy to evaluate the importance of dynamics on the full AD, shallow flows are very sensitive to fluctuations at the time scale selected for this analysis. For example, in RGSSs the shallow, local system supplies much of the water in streams, lakes, and wetlands and at the same time tend to be the focus of development and are more susceptible to contamination. The use of AD to understand these fluctuating systems is subject to large uncertainties, especially when the interpretation of environmental tracers and mathematical models for age is based on the steady flow assumption. On the other hand, the deeper flow systems remain insensitive to fluctuations at the scale used for the forcing, and the traditional steady flow analysis would appear to suffice. In the next section on the full distribution for age we show some important exceptions to this statement. Particularly, we show that for some cases multimodality emerges under transient flow conditions even though the mean age is time invariant.

#### 4.2.2. Averaging Mean Age Over Flow Paths

[60] The total water flux to each discharge zone integrates age across a range of time-varying flow tubes, damping the influence of the forcing fluctuations on discharge ages. In a watershed, such averaging is analogous to observing at a stream or spring that receives contributions from different

flow paths. The flux-weighted dimensionless mean age in discharge zone  $D_i$  is estimated as

$$A_i^*(t) = \frac{1}{T} \frac{\int_{\mathbf{x} \in D_i} [\theta \mathbf{v} a_1(\mathbf{x}, t) - \theta \mathbf{D} \nabla a_1] \cdot \mathbf{n} \, \mathbf{d}\mathbf{x}}{\int_{\mathbf{x} \in D_i} \theta \mathbf{v} \cdot \mathbf{n} \, \mathbf{d}\mathbf{x}}, \quad i = 1, \dots, 5. \quad (31)$$

[61] The relative differences of the flux-weighted dimensionless age across individual discharge zones at the top boundary, for transient and steady flow conditions, is estimated as

$$E_i^a(t) = \left[ \frac{A_i^*(t) - A_{i,s}^*}{A_{i,s}^*} \right] \times 100, \quad (32)$$

which is shown in Figure 6 for three different porosity and hydraulic conductivity depth-decay rates (line colors). These curves are presented for each individual discharge zone and their cumulative response (D1–D5 and Total discharge; columns) and for different fluctuation intensities ( $\beta = 0.1, 0.3, 0.6$ ; rows). Positive (negative) values of  $E_i^a(t)$  correspond to older (younger) mean ages under transient flow conditions. Relative differences vary from  $\pm 2\%$  for small fluctuations with  $\beta = 0.1$  (compared to  $\pm 5\%$  for water flux, not shown) to  $[-30\%, +15\%]$  for large fluctuations with  $\beta = 0.6$  ( $\pm 40\%$  for water flux). The lower amplitude of these relative age differences, compared to differences for water flux, is evidence of the effect of mixing on age. These curves are periodic but asymmetric with minimum and maximum values occurring at different times than those observed for flow. Also unlike flow, their shape depends on the fluctuation intensity  $\beta$ . For example, as the fluctuation intensity increases, the proportion of time with younger mean ages under transient flow (negative values of  $E_i^a(t)$ ) increases for each discharge zone. The extreme values (minimum and maximum) of the relative differences for mean age occur earlier than the extreme values of the relative differences for flow (minimum at  $t/T = 0.5$  and maximum at  $t/T = 0$  or  $t/T = 1$ , not shown); however, as  $\beta$  increases, the time of minimum for mean ages tends to  $t/T = 0.5$ , and the time for maximum remains unchanged. In this case, the mean age at a discharge zone is at its youngest (with respect to steady state) when the flux of water is at a minimum and at its oldest some time before that water flux returns to a maximum. Finally, as depth-decay rate  $A\lambda$  increases, the amplitude of the relative differences decreases (increases) for the discharge zones D1–D3 (D4 and D5) and for the integral over all discharge zones (Figure 6).

[62] Figure 6 also presents the numerical values for the flux-weighted dimensionless mean age under steady flow conditions,  $A_{i,s}^*$  (second row in this figure). Discharge zones D1–D3 have mean ages that decrease with increasing the depth-decay rate  $A\lambda$ . This is consistent with the decrease of contributions from longer flow paths, leading to a dominant role of local flow paths and therefore rejuvenation of waters. On the other hand, discharge zones D4 and D5 have

smaller or null contributions from intermediate flow paths. The decrease in conductivity leads to a decrease in pore velocities and therefore an increase in ages. When the integration is performed over all the discharge zones (last column of Figure 6), the net effect of increasing the depth-decay rate is to decrease the flux-weighted mean ages.

### 4.2.3. Implications for Mean Age

[63] Maps of relative differences for mean ages highlight those zones that strongly respond to temporal changes in forcing (Figure 4). Using the first moment of the AD as a proxy, we observe that the highest-sensitivity zones, which are located below right (upgradient) topographic slopes, are mainly due to shifts in flow direction associated with moving stagnation zones and head boundary maxima (see Figure 5). Applying this observation to dune-induced HZs implies that the greatest age sensitivity to varying flow is below the dune's lee slope. In RGSs we note that watershed modelers often assume that surface-water and groundwater watersheds coincide, ignoring the difference between water-table maxima and groundwater divides (see Figure 2a) and implicitly assuming a static groundwater divide location. Field studies, however, have shown that groundwater divides dynamically respond to changes in climatic conditions, especially in small watersheds [Winter *et al.*, 2003]. These dynamic changes affect flow, age, and the geochemical reactions controlling groundwater chemistry.

[64] Recent work by Jiang *et al.* [2011, 2012] used a Tothian conceptualization, similar to the one used in this study, under steady flow conditions to show that age mass and therefore matter can accumulate around stagnation points, leaving a measurable chemical fingerprint around these locations. Now, under dynamic flow conditions, these low-velocity zones and their capacity to accumulate and transform matter evolve over time and space, leading to larger areas affected by stagnant flow (i.e., a larger chemical fingerprint) and potentially influencing the net solute fluxes within the system, because the inherited dynamics of the stagnation zones results in accumulation and release of chemically evolved waters over time. In other words, the characteristics of the chemical signature found by Jiang *et al.* [2011, 2012] not only depend on where we sample but also when we sample.

[65] Age is recognized as a master variable for biologically and chemically mediated transformations in natural systems. For example, at the scale of hyporheic exchange, the AD has proved to be a fundamental metric to qualify the buffering potential of stream HZs. This metric together with time scales for the biogeochemical reactions of interest allow for the classification of HZs as net sinks or sources of nitrate to the stream [e.g., Gomez *et al.*, 2012; Zarnetske *et al.*, 2012]. Similarly, at the watershed scale, ADs can be used to characterize weathering reactions, secondary mineral precipitation, diagenesis, and metamorphic evolution [e.g., White and Brantley, 2003; Maher, 2010, 2011]. For instance, recent studies by Maher [2010, 2011] used ADs to predict the solute fluxes observed in small watersheds and large river basins. Analogous to the approach used for HZs, these studies use age and the time required to approach chemical equilibrium as dominant controls on solute fluxes. Notice that most studies, including the ones cited here, assume steady flow conditions to characterize the biogeochemical characteristics of

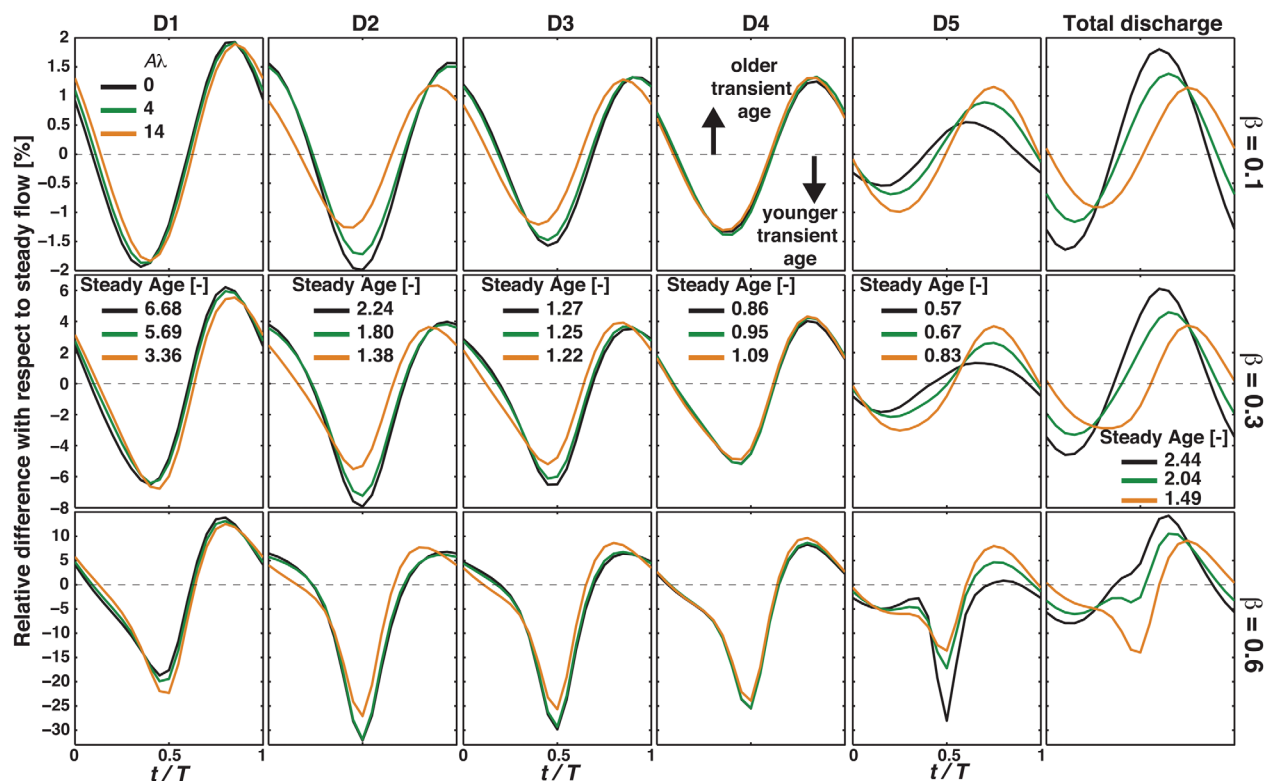


**Figure 6.** Relative difference between the flux-weighted mean age across discharge zones under transient and steady flow conditions ( $E_i^q$ ) over a period  $T$ . Columns correspond to the discharge zones D1–D5, shown in Figure 2a, and flux-weighted age over the entire domain. Rows correspond to different transient fluctuation intensities ( $\beta = 0.1, 0.3$ , and  $0.6$ ). Colors represent different depth-decay rates of porosity and hydraulic conductivity. The second row of each column also presents the dimensionless flux-weighted mean ages (scaled by  $T$ ) estimated under steady flow conditions. ( $X_0/Z_0 = 20, A\lambda = 4, \lambda/\alpha_L = 133.3, \alpha_T/\alpha_L = 0.1$ .)

hydrologic systems; however, under transient flow conditions mean ages and, as shown in more detail in the following section, ADs evolve, changing the state of these systems over time in response to dynamic drivers and therefore affecting the contact time of water relative to the characteristic chemical time scales. Finally, the integrating nature of the discharge boundaries dampens the effect of dynamic forcing on the ADs (Figure 6); this issue is discussed in more detail in the following section.

### 4.3. Age Distributions

[66] We solve equation (15a) for the full distribution of time-varying groundwater age using the change of variables approach (section 2.1.1) and then compare to the distribution for steady flow.

#### 4.3.1. Spatial Patterns of AD

[67] Figure 7 presents the cumulative ADs,  $R$ , for six locations in the domain (P1–P6 in Figure 2a), which correspond to high-sensitivity (P2, P4; i.e., below a right or upgradient slope), moderate-sensitivity (P1, P3; below a discharge area), and low-sensitivity (P5, P6; regional) zones according to Figure 4. ADs are estimated for three different fluctuation intensities ( $\beta = 0.1, 0.3, 0.6$ ), and for each case, graphs of cumulative ADs ( $R$ ) for steady (black line) and transient (colored lines) flow conditions are superimposed. To the right of these graphs are filled contour

plots of the cumulative AD as a function of dimensionless time ( $t/T$ ) and age ( $\tau/T$ ). The contour plots with more blue, found toward the bottom of Figure 7, represent older ages. Those with broader transition between blue and red, like P3, have a larger range of ages. The contour surfaces also help identify temporal fluctuations of the ADs. Those with nonstationary color transitions, like P2 for all values of  $\beta$ , indicate sensitivity to the important role of flow dynamics on the time evolution of ADs, while for P6 the traces are time invariant and insensitive to dynamics. Also, shown for each case is an inset of the AD, as  $\rho$ , for steady flow (red line) and for transient flow at  $t/T = 0.5$  (gray bars). The inset ADs help identify characteristic times using  $\rho$ , since for  $R$  these are associated with slope discontinuities that are difficult to see.

[68] Within local flow systems there are locations for which ADs, like the mean ages in the last section, are relatively insensitive to dynamic forcing, such as P1 which is situated under a discharge area. Other locations, especially when situated below a right (upgradient) slope, like location P2, are very sensitive and respond strongly. For example, the graph and contour plot for P2 demonstrate significant variability along the time axis, including variability of its characteristic time scale (the mode of the distribution) and mean (see contour and inset ADs for P2), even for small  $\beta$ . As we move deeper in the system; for

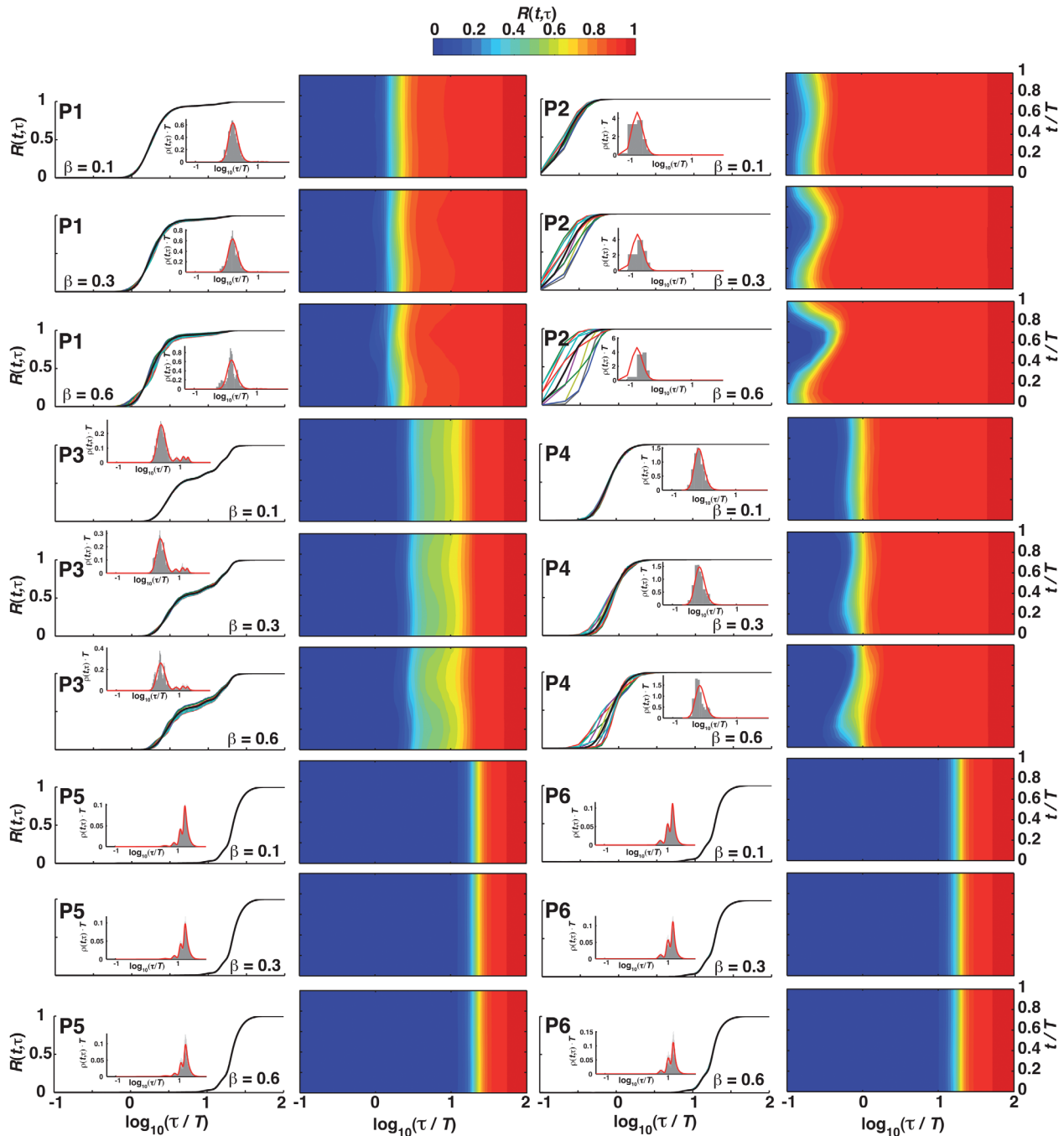


**Figure 7.** Cumulative AD  $R(t, \tau)$  at locations P1–P6 (see Figure 2) for intensities  $\beta = 0.1, 0.3,$  and  $0.6$ . For each location and intensity  $\beta$ , the cumulative distributions under steady (black line) and transient (colored lines) flow are superimposed on the left side, while the surface on the right corresponds to the temporal (vertical axis) evolution of the cumulative AD as a function of age (horizontal axis). An inset of the AD under steady flow (red line) and transient flow at  $t/T = 0.5$  (gray bars) is also presented. ( $X_0/Z_0 = 20, A\lambda = 4, \lambda/\alpha_l = 133.3, \alpha_T/\alpha_L = 0.1$ .)

example, to points P3–P6, there is less temporal variation of ADs. Larger fluctuations in the forcing are required to obtain any noticeable change in the intermediate flow systems (such as P3, although fluctuations do not have to be as large for the more sensitive P4 located under the right slope), while points located in regional flow system (P5, P6) are invariant to the transient forcing.

[69] Under steady flow conditions the ADs for the local flow system (e.g., P1 and P2) have only one characteristic time scale (a single slope discontinuity in the cumulative AD; one mode or peak in the inset ADs), but multiple modes appear deeper in the system, for both intermediate flow (P3, four peaks; but one at P4) and regional flow (P5, P6; three peaks each).

[70] Under dynamic forcing, multimodality and new characteristic time scales also emerge in the local flow system, when the fluctuations are sufficiently large, with two peaks at P1 for  $\beta = 0.3$  and three for  $\beta = 0.6$ , although the mean does not change. Additional modes and characteristic time scales also emerge in intermediate flow, with modes at P3 increasing from four to six, and P4 getting a second mode. The modes in the regional system do not change with dynamic forcing. In summary, locations within intermediate and regional flow systems, or locations in local systems close to discharge zones, are prone to mixing effects that lead to more than one characteristic time scale, especially under dynamic forcing. One interesting result is that the most sensitive of the six locations, P2, is the only one to always be characterized by a unimodal distribution, while the next most sensitive location, P4, becomes bimodal only for the largest forcing fluctuation. These locations are below a right (upgradient) slope (Figure 2a) and well away from a stagnation zone (Figure 3), in an area where flow direction does not vary much (Figure 5).

[71] Moments of the AD (e.g., mean or variance) adequately characterize the distribution only when there is a single mode. The emergence of multimodality with transient flows means that moments are no longer sufficient. In other words, the mean of the AD is a misleading metric under transient flow conditions. The shape of the distribution and the scales of importance evolve over time even while the mean remains time invariant (e.g., P2). Environmental tracers are used to estimate the mean age, but they are actually a weighted value of the AD; this estimate can be quite different from the mean, and even if it is close, the mean does not capture the characteristic time scales, especially for a multimodal distribution, making it difficult to reconstruct the full AD from environmental tracer observations.

#### 4.3.2. Averaging AD Over Flow Paths

[72] Figure 8 presents the flux-weighted cumulative ADs for the five discharge zones under different forcing intensities  $\beta$ . The flux-weighted AD  $\rho_i$  or its cumulative  $R_i$  at the discharge zone  $D_i$  is estimated as

$$\zeta_i(\mathbf{x}, t, \tau) = \frac{\int_{\mathbf{x} \in D_i} [\theta \mathbf{v} \zeta(\mathbf{x}, t, \tau) - \theta \mathbf{D} \nabla \zeta(\mathbf{x}, t, \tau)] \cdot \mathbf{n} \, d\mathbf{x}}{\int_{\mathbf{x} \in D_i} \theta \mathbf{v} \cdot \mathbf{n} \, d\mathbf{x}}; \quad (33)$$

$$\zeta = \rho, R; i = 1, \dots, 5.$$

[73] The information presented in Figure 8 is similar to the one presented in Figure 7, where an inset of the flux-weighted AD  $\rho_i$  for steady flow (red line) and transient flow at  $t/T = 0.5$  (gray bars) is also included.

[74] In general, all discharge zones demonstrate temporal variability of AD, even for small  $\beta$ . Although the functional form remains stationary, the characteristic time scale (mode) and the mean evolve. Variability is subtle for small temporal fluctuations ( $\beta = 0.1$ ) but progressively increases as forcing intensity increases ( $\beta = 0.3$ ), until it reaches an asymptote above  $\beta = 0.3$  (posteriorly validated with the analyses of the envelope of the cumulative ADs under transient flow conditions; not shown). This asymptotic convergence is not present at the local scale (P1–P6), where

increases in  $\beta$  lead to continuous increases in the temporal variability of the AD. Integration over discharge zones is equivalent to averaging over several flow paths, leading to the less variability in the functional form of the AD. Moreover, averaging over several flow paths results in either unimodality (D1 and D2) or bimodality (D3–D5), in contrast to the multimodal behavior observed at the local scale close to the discharge zone (e.g., points P1 with three modes under transient flow conditions and P3 with four and six modes under steady and transient flow conditions, respectively). This behavior at the discharge zones can be explained by a flow field that favors younger water (local flow systems), and therefore the moments become a good tool to describe these distributions.

#### 4.3.3. Implications for AD

[75] In general, dynamic forcing plays a key role in the shape of the flow field (see Figure 2), which at the same time induces mixing and affects the role of advection and dispersion, producing broader, more variable, and multimodal ADs. This behavior is evidence of the uncertainty introduced by the steady flow assumption in both age modeling and data interpretation by which important characteristic time scales and multimodality are ignored.

[76] Even though the first moment of the AD (mean age) is a useful and relatively easy to model metric to evaluate the role of flow dynamics in the ADs, it can disguise important emerging characteristics such as multimodality. There are locations in the system where flow dynamics does not affect the mean ages (e.g., locations P1 and P3), even for large fluctuation intensities. However, these locations present multiple emergent peaks in the AD (multimodality) even while the mean age remains constant, having important implications for the biogeochemical processes taking place and the interpretation of environmental tracers. Moreover, if we are interested in the AD and its characteristic time scales as a proxy to understand the range of possible biochemical transformation in the system, sampling at the discharge zones (e.g., rivers at the watershed scale) disguises the effects of multimodality and therefore the possibility of identifying processes that correlate with the missing time scales. Averaging over flow paths gives the impression that the system has a unique characteristic time scale (two in some cases), even though the actual system is actually characterized by a nested system of important scales. In RGSs this suggests that a sample taken from a stream, which represents the average of many flow paths, and a sample taken from a nearby well or tributary spring, which would represent a smaller subset of flow paths, could have significantly different ADs and modality.

[77] *Cardenas and Jiang* [2010] present a detailed analysis of the effects that systematic changes in regional and local heterogeneities have on the flow, transport, and ADs for a Tothian, steady flow system. They found that regional changes in heterogeneity, represented by the exponential decay in porosity and conductivity, enhance shallow circulation systems and diminish flow along deep and regional flow systems. Our work presents a similar behavior since the same type of heterogeneities are considered; however, transience modulates changes in flushing times by temporarily increasing (or decreasing) the flux and penetration of shallow flow system. In other words, we incorporate the steady effect of heterogeneity and add a dynamic factor,

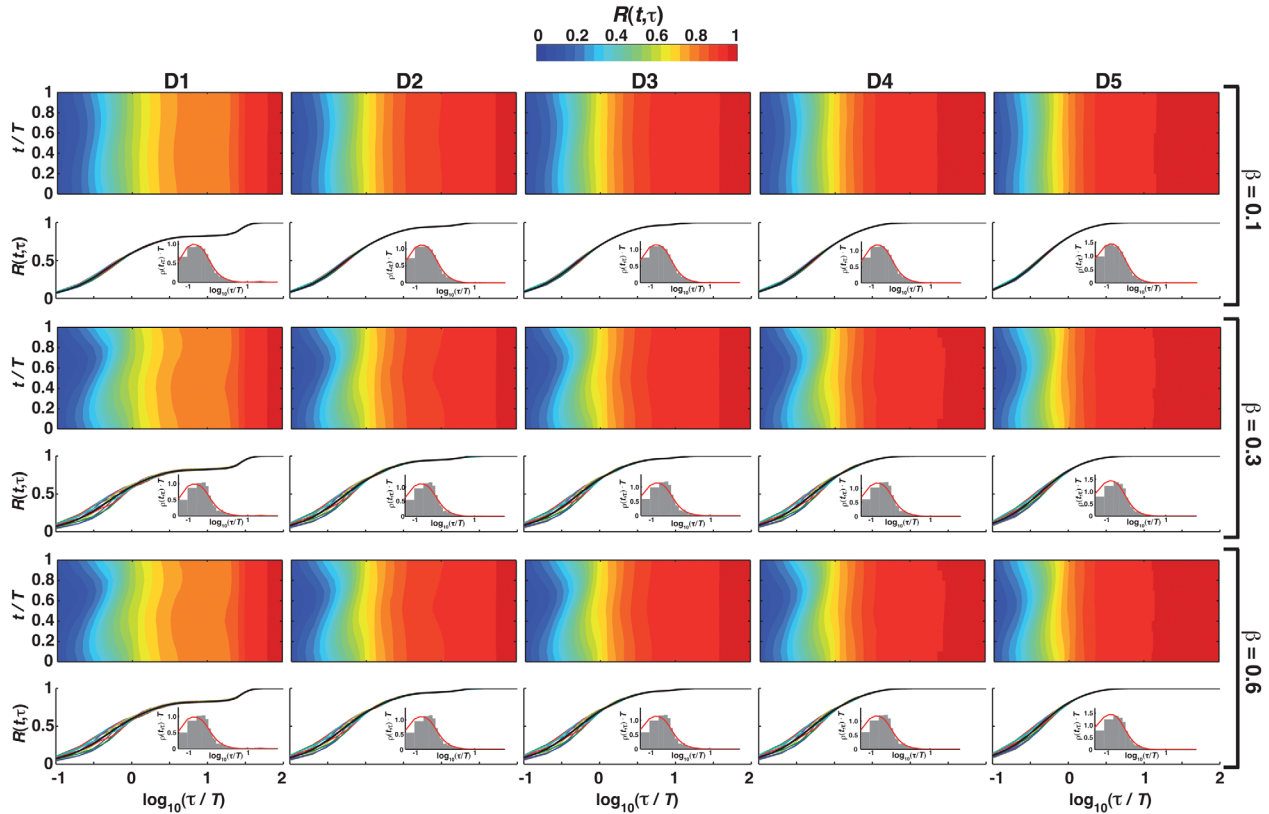


**Figure 8.** Cumulative AD  $R(t, \tau)$  at discharge zones D1–D5 (see Figure 2) for intensities  $\beta = 0.1, 0.3$ , and  $0.6$ . For each discharge zone and intensity  $\beta$ , the surface on the top corresponds to the temporal (vertical axis) evolution of the cumulative AD as a function of age (horizontal axis), while the cumulative distributions under steady (black line) and transient (colored lines) flow are superimposed on the bottom. An inset of the AD under steady flow (red line) and transient flow at  $t/T = 0.5$  (gray bars) is also presented. ( $X_0/Z_0 = 20, A\lambda = 4, \lambda/\alpha_L = 133.3, \alpha_T/\alpha_L = 0.1$ .)

which expands and contracts the local, intermediate, and regional flow systems and is reflected in the temporal evolution of the ADs at the discharge zones (Figures 6 and 8). It is important to notice that these changes are not strong enough to considerably change the late-time behavior (i.e., tailing) of the ADs (Figure 8). Future work will address this aspect in more detail.

## 5. Conclusions

[78] Measuring and modeling of groundwater age have become important tools for the understanding of groundwater systems. However, steady flow remains an implicit assumption for both the interpretation of environmental tracers and modeling of groundwater ages. Natural and human-induced variabilities in hydrologic forcings lead to dynamic flow fields that together with mixing, caused by diffusion and dispersion, shape the ADs of natural systems. The topography-driven system used in the example mimics the nested scales of exchange observed in many natural systems. Particularly, it demonstrates the importance of flow dynamics on ADs for local flow systems (shallow flow paths) and the emergence of new modes in the AD under transient flow conditions. It is worth noticing that the importance of dynamic forcing depends on the intensity of its fluctuation (represented by  $\beta$  in our conceptual model). For

example, for small fluctuations ( $\beta = 0.1$ ) such as expected in most regional aquifers, the traditional steady flow assumption may be adequate. In that case it would not miss important changes in the modeled ADs or measured environmental tracer ages. However, greater fluctuation intensity ( $\beta = 0.3$ ), still within the range observed in a RGS, leads to important changes in modeled ADs and the environmental tracer ages, overpassing the limits of acceptability of steady flow assumptions. On a similar note, HZs are commonly exposed to the largest fluctuation intensities used in this modeling effort; these systems are expected to have important changes in ADs due to dynamic flow conditions. These findings urge a change of gears in terms of the tools used for modeling as well as for the interpretation of natural and artificial tracers.

[79] One of the reasons for maintaining the steady flow assumption is the considerable amount of effort necessary to account for time variant ADs. To capture the temporal evolution of ADs requires modeling of the system's transient flow field, which is more challenging in terms of the numerical schemes used and the amount of data required. It also requires the posterior solution of a sequence of independent advection-dispersion problems. Future work needs to focus on the implementation of adequate mathematical and numerical techniques that allow for the easy implementation of the modeling tools described in this work, and

to use these tools in sampling design and data interpretation. The ability to decompose this complex 5-D problem into independent 4-D cases (see sections 2.1.1 and 2.1.2) allows us to efficiently use high-performance computing for real applications in three spatial dimensions. Also, of particular interest is the introduction of new conceptual models for the interpretation of environmental tracers that account for this dynamic behavior.

[80] **Acknowledgments.** This research was funded by the National Science Foundation through the New Mexico EPSCoR Track I–II (award EAR 0814449), the project Dynamic Groundwater Age Distributions: Exploring Watershed Scale Subsurface Systems (award EAR 1015100), and the grants AGU Horton Research Grant and New Mexico Water Resources Research Institute Student Grant awarded to J.D.G. The authors thank William Stone at New Mexico Tech and Matthew N. Baillie of Kennedy/Jenks consultants in San Francisco, California, for their valuable suggestions regarding this paper. Finally, the writers also thank the Editors, Timothy R. Ginn, Xiao-Wei Jiang, and an anonymous reviewer for providing constructive comments that greatly improved this paper.

## References

- Alley, W., R. Healy, J. LaBaugh, and T. Reilly (2002), Hydrology—Flow and storage in groundwater systems, *Science*, 296(5575), 1985–1990.
- Anderson, W. P., and R. E. Emanuel (2008), Effect of interannual and interdecadal climate oscillations on groundwater in North Carolina, *Geophys. Res. Lett.*, 35, L23402, doi:10.1029/2008GL036054.
- Barco, J., T. S. Hogue, M. Giroto, D. R. Kendall, and M. Putti (2010), Climate signal propagation in southern California aquifers, *Water Resour. Res.*, 46, W00F05, doi:10.1029/2009WR008376.
- Bear, J. (1972), *Dynamics of Fluids in Porous Media*, Elsevier, New York.
- Bethke, C., and T. Johnson (2002), Paradox of groundwater age, *Geology*, 30(4), 385–388.
- Bethke, C. M., and T. M. Johnson (2008), Groundwater age and groundwater age dating, *Annu. Rev. Earth Planet. Sci.*, 36, 121–152, doi:10.1146/annurev.earth.36.031207.124210.
- Boano, F., R. Revellia, and L. Ridolfi (2010), Effect of streamflow stochasticity on bedform-driven hyporheic exchange, *Adv. Water Resour.*, 33, 1367–1374, doi:10.1016/j.advwatres.2010.03.005.
- Bolin, B., and H. Rodhe (1973), A note on the concepts of age distribution and transit time in natural reservoirs, *Tellus*, 25, 58–62.
- Boupha, K., J. Jacobs, and K. Hatfield (2004), Mdl groundwater software: Laplace transforms and the de Hoog algorithm to solve contaminant transport equations, *Comput. Geosci.*, 30(5), 445–453, doi:10.1016/j.cageo.2004.02.001.
- Campana, M. E. (1987), Generation of ground-water age distributions, *Ground Water*, 25(1), 51–58.
- Cardenas, M. B. (2007), Potential contribution of topography-driven regional groundwater flow to fractal stream chemistry: Residence time distribution analysis of Toth flow, *Geophys. Res. Lett.*, 34, L05403, doi:10.1029/2006GL029126.
- Cardenas, M. B., and X.-W. Jiang (2010), Groundwater flow, transport, and residence times through topography-driven basins with exponentially decreasing permeability and porosity, *Water Resour. Res.*, 46, W11538, doi:10.1029/2010WR009370.
- Cardenas, M. B., and J. L. Wilson (2007a), Hydrodynamics of coupled flow above and below a sediment–water interface with triangular bedforms, *Adv. Water Resour.*, 30, 301–313, doi:10.1016/j.advwatres.2006.06.009.
- Cardenas, M. B., and J. L. Wilson (2007b), Dunes, turbulent eddies, and interfacial exchange with permeable sediments, *Water Resour. Res.*, 43, W08412, doi:10.1029/2006WR005787.
- Charbeneau, R. J. (2000), *Groundwater Hydraulics and Pollutant Transport*, Prentice Hall Upper Saddle River, N. J.
- Cirpka, O. A., and S. Attinger (2003), Effective dispersion in heterogeneous media under random transient flow conditions, *Water Resour. Res.*, 39(9), 1257, doi:10.1029/2002WR001931.
- Clark, I. D., and P. Fritz (1997), *Environmental Isotopes in Hydrogeology*, CRC Press., Boca Raton, Fla.
- Cornaton, F., and P. Perrochet (2006a), Groundwater age, life expectancy and transit time distributions in advective-dispersive systems: 1. Generalized reservoir theory, *Adv. Water Resour.*, 29(9), 1267–1291, doi:10.1016/j.advwatres.2005.10.009.
- Cornaton, F., and P. Perrochet (2006b), Groundwater age, life expectancy and transit time distributions in advective-dispersive systems: 2. Reservoir theory for sub-drainage basins, *Adv. Water Resour.*, 29(9), 1292–1305, doi:10.1016/j.advwatres.2005.10.010.
- Cornaton, F. J. (2012), Transient water age distributions in environmental flow systems: The time-marching Laplace transform solution technique, *Water Resour. Res.*, 48, W03524, doi:10.1029/2011WR010606.
- de Hoog, F. R., J. H. Knight, and A. N. Stokes (1982), An improved method for numerical inversion of Laplace transforms, *Siam J. Sci. Stat. Comput.*, 3(3), 357–366.
- Deleersnijder, E., J.-M. Campin, and E. J. M. Delhez (2001), The concept of age in marine modelling: I. Theory and preliminary model results, *J. Mar. Syst.*, 28(3–4), 229–267, doi:10.1016/S0924-7963(01)00026-4.
- Delhez, E. J. M., J. M. Delhez, and E. Deleersnijder (2002), The concept of age in marine modelling: II. concentration distribution function in the English channel and the North Sea, *J. Mar. Syst.*, 31(4), 279–297, doi:10.1016/S0924-7963(01)00066-5.
- Elliott, A. H., and N. H. Brooks (1997a), Transfer of nonsorbing solutes to a streambed with bed forms: Theory, *Water Resour. Res.*, 33(1), 123–136.
- Elliott, A. H., and N. H. Brooks (1997b), Transfer of nonsorbing solutes to a streambed with bed forms: Laboratory experiments, *Water Resour. Res.*, 35(1), 137–151.
- Engdahl, N. B., T. R. Ginn, and G. E. Fogg (2012), Non-Fickian dispersion of groundwater age, *Water Resour. Res.*, 48, W07508, doi:10.1029/2012WR012251.
- Etcheverry, D., and P. Perrochet (2000), Direct simulation of groundwater transit-time distributions using the reservoir theory, *Hydrogeol. J.*, 8(2), 200–208.
- Fehlman, H. M. (1985), Resistance components and velocity distributions of open channel flows over bedforms, Master's dissertation, Colo. State Univ., Fort Collins.
- Fiori, A., and D. Russo (2008), Travel time distribution in a hillslope: Insight from numerical simulations, *Water Resour. Res.*, 44, W12426, doi:10.1029/2008WR007135.
- Fogg, G. E., E. M. LaBolle, and G. S. Weissmann (1999), Groundwater vulnerability assessment: Hydrogeologic perspective and example from Salinas Valley, California, in *Assessment of Non-Point Source Pollution in the Vadose Zone*, *Geophys. Monogr. Ser.*, vol. 108, edited by D. L. Corwin, K. Loague, and T. R. Ellsworth, pp. 45–61, AGU, Washington, D. C.
- Fogler, H. S. (2006), *Elements of Chemical Reaction Engineering*, Prentice Hall PTR International Series in the Physical and Chemical Engineering Sciences, 4th ed., Prentice Hall PTR, Upper Saddle River, N. J.
- Freeze, R. A., and P. A. Witherspoon (1966), Theoretical analysis of regional groundwater flow: 1. Analytical and numerical solutions to the mathematical model, *Water Resour. Res.*, 2(4), 641–656, doi:10.1029/WR002i004p00641.
- Freeze, R. A., and P. A. Witherspoon (1967), Theoretical analysis of regional groundwater flow: 2. Effect of water-table configuration and subsurface permeability variation, *Water Resour. Res.*, 3(2), 623–634, doi:10.1029/WR003i002p00623.
- Gelhar, L., C. Welty, and K. Rehfeldt (1992), A critical review of data on field-scale dispersion in aquifers, *Water Resour. Res.*, 28(7), 1955–1974.
- Ginn, T. R. (1999), On the distribution of multicomponent mixtures over generalized exposure time in subsurface flow and reactive transport: Foundations, and formulations for groundwater age, chemical heterogeneity, and biodegradation, *Water Resour. Res.*, 35(5), 1395–1407.
- Ginn, T. R., H. Haeri, A. Massoudieh, and L. Foglia (2009), Notes on groundwater age in forward and inverse modeling, *Transp. Porous Media*, 79(1), 117–134, doi:10.1007/s11242-009-9406-1.
- Gleeson, T., and A. H. Manning (2008), Regional groundwater flow in mountainous terrain: Three-dimensional simulations of topographic and hydrogeologic controls, *Water Resour. Res.*, 44, W10403, doi:10.1029/2008WR006848.
- Gomez, J. D., and J. L. Wilson (2010), Effects of flow dynamics on age distributions, Abstract H31J-07 presented at 2010 Fall Meeting, AGU.
- Gomez, J. D., J. L. Wilson, and M. B. Cardenas (2012), Residence time distributions in sinuosity-driven hyporheic zones and their biogeochemical effects, *Water Resour. Res.*, 48, W09533, doi:10.1029/2012WR012180.
- Goode, D. (1996), Direct simulation of groundwater age, *Water Resour. Res.*, 32(2), 289–296.
- Goode, D., and L. Konikow (1990), Apparent dispersion in transient groundwater flow, *Water Resour. Res.*, 26(10), 2339–2351.
- Goode, D. J. (1998), Groundwater age and atmospheric tracers: Simulation studies and analysis of field data from the Mirror Lake site, New

- Hampshire, Ph.D. dissertation, Dep. Civ. Eng. and Oper. Res., Princeton Univ., Princeton, N. J.
- Goode, D. J. (1999), Age, double porosity, and simple reaction modifications for the MOC3D ground-water transport model, Water-Resour. Invest. Rep. 99-4041, U.S. Geol. Surv., Reston, Va.
- Gurtin, M. E., and R. C. MacCamy (1974), Non-linear age-dependent population dynamics, *Arch. Ration. Mech. Anal.*, 54(3), 281-300.
- Haggerty, R., S. Wondzell, and M. Johnson (2002), Power-law residence time distribution in the hyporheic zone of a 2nd-order mountain stream, *Geophys. Res. Lett.*, 29(13), 1640, doi:10.1029/2002GL014743.
- Haine, T., and T. Hall (2002), A generalized transport theory: Water-mass composition and age, *J. Phys. Oceanogr.*, 32(6), 1932-1946.
- Haine, T. W. N., H. Zhang, D. W. Waugh, and M. Holzer (2008), On transit-time distributions in unsteady circulation models, *Ocean Model.*, 21(1-2), 35-45, doi:10.1016/j.ocemod.2007.11.004.
- Hall, T., and R. Plumb (1994), Age as a diagnostic of stratospheric transport, *J. Geophys. Res.—Atmos.*, 99(D1), 1059-1070.
- Harvey, J. W., and K. E. Bencala (1993), The effect of streambed topography on surface-subsurface water exchange in mountain catchments, *Water Resour. Res.*, 29(1), 89-98.
- Holzer, M., and T. Hall (2000), Transit-time and tracer-age distributions in geophysical flows, *J. Atmos. Sci.*, 57(21), 3539-3558.
- Ingebritsen, S., and C. Manning (1999), Geological implications of a permeability-depth curve for the continental crust, *Geology*, 27(12), 1107-1110.
- Jiang, X.-W., L. Wan, X.-S. Wang, S. Ge, and J. Liu (2009), Effect of exponential decay in hydraulic conductivity with depth on regional groundwater flow, *Geophys. Res. Lett.*, 36, L24402, doi:10.1029/2009GL041251.
- Jiang, X.-W., X.-S. Wang, and L. Wan (2010a), Semi-empirical equations for the systematic decrease in permeability with depth in porous and fractured media, *Hydrogeol. J.*, 18(4), 839-850, doi:10.1007/s10040-010-0575-3.
- Jiang, X.-W., L. Wan, M. B. Cardenas, S. Ge, and X.-S. Wang (2010b), Simultaneous rejuvenation and aging of groundwater in basins due to depth-decaying hydraulic conductivity and porosity, *Geophys. Res. Lett.*, 37, L05403, doi:10.1029/2010GL042387.
- Jiang, X. W., X. S. Wang, L. Wan, and S. Ge (2011), An analytical study on stagnant points in nested flow systems in basins with depth-decaying hydraulic conductivity, *Water Resour. Res.*, 47, W01512, doi:10.1029/2010WR009346.
- Jiang, X.-W., L. Wan, S. Ge, G.-L. Cao, G.-C. Hou, F.-S. Hu, X.-S. Wang, H. Li, and S.-H. Liang (2012), A quantitative study on accumulation of age mass around stagnation points in nested flow systems, *Water Resour. Res.*, 48, W12502, doi:10.1029/2012WR012509.
- Jury, W. A., and K. Roth (1990), *Transfer Functions and Solute Movement Through Soil: Theory and Applications*, Birkhäuser Verl., Basel.
- Kazemi, G. A., J. H. Lehr, and P. Perrochet (2006), *Groundwater Age*, Wiley-Interscience, Hoboken, N. J.
- Maher, K. (2010), The dependence of chemical weathering rates on fluid residence time, *Earth Planet. Sci. Lett.*, 294, 101-110, doi:10.1016/j.epsl.2010.03.010.
- Maher, K. (2011), The role of fluid residence time and topographic scales in determining chemical fluxes from landscapes, *Earth Planet. Sci. Lett.*, 312, 48-58, doi:10.1016/j.epsl.2011.09.040.
- Massoudieh, A., and T. R. Ginn (2011), The theoretical relation between unstable solutes and groundwater age, *Water Resour. Res.*, 47, W10523, doi:10.1029/2010WR010039.
- McGuire, K. J., and J. J. McDonnell (2006), A review and evaluation of catchment transit time modeling, *J. Hydrol.*, 330(3-4), 543-563, doi:10.1016/j.jhydrol.2006.04.020.
- Ophori, D., and J. Toth (1990), Influence of the location of production wells in unconfined groundwater basins: An analysis by numerical simulation, *Can. J. Earth Sci.*, 27(5), 657-668.
- Phillips, F. M., and M. C. Castro (2003), Groundwater dating and residence time measurements, in *Treatise on Geochemistry*, vol. 5, edited by J. I. Drever, pp. 451-497, Oxford Univ. Press, Oxford.
- Phillips, F. M., M. A. Walvoord, and E. E. Small (2004), Effects of environmental change on groundwater recharge in desert southwest, in *Groundwater Recharge in a Desert Environment: The Southwestern United States*, edited by F. M. Phillips, J. F. Hogan, and B. Scanlon, pp. 273-293, AGU, Washington, D. C.
- Pint, C. D., R. J. Hunt, and M. P. Anderson (2003), Flowpath delineation and ground water age, Allequash basin, Wisconsin, *Ground Water*, 41(7), 895-902, doi:10.1111/j.1745-6584.2003.tb02432.x.
- Price, R. M., Z. Top, J. D. Happell, and P. K. Swart (2003), Use of tritium and helium to define groundwater flow conditions in everglades national park, *Water Resour. Res.*, 39(9), 1267, doi:10.1029/2002WR001929.
- Prommer, H., D. Barry, and G. Davis (2002), Modelling of physical and reactive processes during biodegradation of a hydrocarbon plume under transient groundwater flow conditions, *J. Contam. Hydrol.*, 59, 113-131.
- Rotenberg, M. (1972), Theory of population transport, *J. Theor. Biol.*, 37, 291-305.
- Schirmer, M., G. Durrant, J. Molson, and E. Frind (2001), Influence of transient flow on contaminant biodegradation, *Ground Water*, 39(2), 276-282.
- SchulzeMakuch, D. (2005), Longitudinal dispersivity data and implications for scaling behavior, *Ground Water*, 43(3), 443-456.
- Sophocleous, M. (2002), Interactions between groundwater and surface water: The state of the science, *Hydrogeol. J.*, 10(1), 52-67, doi:10.1007/s10040-001-0170-8.
- Sturchio, N. C., et al. (2004), One million year old groundwater in the Sahara revealed by krypton-81 and chlorine-36, *Geophys. Res. Lett.*, 31(5), doi:10.1029/2003GL019234.
- Sudicky, E. A. (1989), The Laplace transform Galerkin technique: A time continuous finite element theory and application to mass transport in groundwater, *Water Resour. Res.*, 25(8), 1833-1846.
- Tóth, J. (1962), A theory of groundwater motion in small drainage basins in central Alberta, *J. Geophys. Res.*, 67, 4375-4387.
- Tóth, J. (1963), An analysis of groundwater flow in a finite region with a sinusoidal top, *J. Geophys. Res.*, 68, 4795-4812.
- Tóth, J. (2009), *Gravitational Systems of Groundwater Flow: Theory, Evaluation, Utilization*, Cambridge Univ. Press, Cambridge.
- Trucco, E. (1965), Mathematical models for cellular systems the Von Foerster equation. Part I, *Bull. Math. Biol.*, 27(3), 285-304, doi:10.1007/BF02478406.
- Varni, M., and J. Carrera (1998), Simulation of groundwater age distributions, *Water Resour. Res.*, 34(12), 3271-3281.
- Weissmann, G. S., Y. Zhang, E. M. LaBolle, and G. E. Fogg (2002), Dispersion of groundwater age in an alluvial aquifer system, *Water Resour. Res.*, 38(10), doi:10.1029/2001WR000907.
- White, A. F., and S. L. Brantley (2003), The effect of time on the weathering of silicate minerals: Why do weathering rates differ in the laboratory and field?, *Chem. Geol.*, 202, 479-506.
- Winter, T. C., D. O. Rosenberry, and J. W. LaBaugh (2003), Where does the ground water in small watersheds come from?, *Ground Water*, 41(7), 989-1000.
- Wood, B., and M. Kavvas (1999a), Ensemble-averaged equations for reactive transport in porous media under unsteady flow conditions, *Water Resour. Res.*, 35(7), 2053-2068, doi:10.1029/1999WR900113.
- Wood, B. D., and M. L. Kavvas (1999b), Stochastic solute transport under unsteady flow conditions: Comparison of theory, Monte Carlo simulations, and field data, *Water Resour. Res.*, 35(7), 2069-2084, doi:10.1029/1999WR900112.
- Woolfenden, L. R., and T. R. Ginn (2009), Modeled ground water age distributions, *Ground Water*, 47(4), 547-557, doi:10.1111/j.1745-6584.2008.00550.x.
- Xu, Y., and H. F. Beekman (2003), *Groundwater Recharge Estimation in Southern Africa*, vol. UNESCO IHP Ser. 64, UNESCO, Paris.
- Zarnetske, J. P., R. Haggerty, S. M. Wondzell, V. A. Bokil, and R. Gonzalez-Pinzon (2012), Coupled transport and reaction kinetics control the nitrate source-sink function of hyporheic zones, *Water Resour. Res.*, 48, W11508, doi:10.1029/2012WR011894.
- Zijl, W. (1999), Scale aspects of groundwater flow and transport systems, *Hydrogeol. J.*, 7(1), 139-150.
- Zinn, B. A., and L. Konikow (2007a), Effects of intraborehole flow on groundwater age distribution, *Hydrogeol. J.*, 15, 633-643, doi:10.1007/s10040-006-0139-8.
- Zinn, B. A., and L. F. Konikow (2007b), Potential effects of regional pumping on groundwater age distribution, *Water Resour. Res.*, 43, W06418, doi:10.1029/2006WR004865.
- Zongyu, C., N. Zhenlong, Z. Zhaoji, Q. Jixiang, and N. Yunju (2005), Isotopes and sustainability of ground water resources, north china plain, *Ground Water*, 43(4), 485-493.